Journal of Chromatography A, 1218 (2011) 3447–3452

Contents lists available at ScienceDirect

Journal of Chromatography A

journal homepage: www.elsevier.com/locate/chroma

Liquid chromatographic separation of proteins derivatized with a fluorogenic reagent at cysteinyl residues on a non-porous column for differential proteomics analysis

Akiyo Koshiyama[a], Tomoko Ichibangase[a], Kyoji Moriya[b], Kazuhiko Koike[c], Itaru Yazawa[d], Kazuhiro Imai[a,*]

[a] Research Institute of Pharmaceutical Sciences, Musashino University, 1-1-20 Shinmachi, Nishitokyo-shi, Tokyo 202-8585, Japan
[b] Department of Infection Control and Prevention, Graduate School of Medicine, University of Tokyo, 7-3-1 Hongo, Bunkyo-ku, Tokyo 113-8655, Japan
[c] Department of Internal Medicine, Graduate School of Medicine, University of Tokyo, 7-3-1 Hongo, Bunkyo-ku, Tokyo 113-8655, Japan
[d] Imtakt Corporation, Kyoto Research Park, Chudoji Minami, Shimogyo-ku, Kyoto 600-8813, Japan

ARTICLE INFO

Article history:
Received 1 February 2011
Received in revised form 24 March 2011
Accepted 26 March 2011
Available online 4 April 2011

Keywords:
FD–LC–MS/MS method
Non-porous column
Wide-pore column
Differential proteomics analysis
Hepatocarcinogenesis

ABSTRACT

A wide-pore (30 nm) reversed-phase column (Intrada WP-RP, particle size 3 μm) was recently utilized for protein separation in differential proteomics analysis with fluorogenic derivatization-liquid chromatography–tandem mass spectrometry (FD–LC–MS/MS), and exerted a tremendous effect on finding biomarkers (e.g., for breast cancer). Further high-performance separation is required for highly complex protein mixtures. A recently prepared non-porous small-particle reversed-phase column (Presto FF-C18, particle size: 2 μm) was expected to more effectively separate derivatized protein mixtures than the wide-pore column. A preliminary experiment demonstrated that the peak capacity of the former was threefold greater than that of the latter in gradient elution of a fluorogenic derivatized model peptide, calcitonin. The FD–LC–MS/MS method with a non-porous column was then optimized and applied to separate liver mitochondrial proteins that were not efficiently separated with the wide-pore column. As a result, high-performance separation of mitochondrial proteins was accomplished, and differential proteomics analysis of liver mitochondrial proteins in a hepatitis-infected mouse model was achieved using the FD–LC–MS/MS method with the non-porous column. This result suggests the non-porous small-particle column as a replacement for the wide-pore column for differential proteomics analysis in the FD–LC–MS/MS method.

© 2011 Elsevier B.V. All rights reserved.

1. Introduction

High-performance liquid chromatography (HPLC) has been used for separating highly complex mixtures of compounds, such as cell and tissue extracts. However, because efficient separation of intact proteins is difficult, one-dimensional (1D) or multidimensional (mD) HPLC is usually performed with peptides generated by digesting intact proteins in proteomics analysis (reviewed in Ref. [1]). In contrast, we have developed the first reproducible quantification method using 1D HPLC for proteomics analysis, called fluorogenic derivatization-liquid chromatography-tandem mass spectrometry (FD–LC–MS/MS) with a database-searching algorithm. Intact protein mixtures were first derivatized at cysteinyl residues with a fluorogenic reagent, followed by isolation with a wide-pore reversed-phase column, Intrada WP-RP (30 nm pore size and 3 μm particle) (Imtakt, Kyoto, Japan), digestion of the derivatized proteins, and identification of the isolated proteins [2]. Application to real biological samples indicated the appearance of more than 400 or 500 proteins on a chromatogram [3–7]. Differential proteomics analysis demonstrated the existence of many proteins related to an early stage of Parkinson's disease [3], developmental stages of hepatocarcinogenesis [4], metastatic or normal breast cancer cells [5], the aging of rat brain regions [6], and the running speed of horses [7].

Differential proteomics analysis of liver proteins between hepatitis C virus (HCV) core gene transgenic (Tg) and non-transgenic (NTg) mice indicated some disease-related proteins in the developmental stages of hepatocarcinogenesis [4]. Since many of those proteins were related to the function of mitochondrial events (e.g., respiration, electron-transfer system, and β-oxidation), we further performed differential proteomics analysis of liver mitochondrial proteins between Tg and NTg mice by FD–LC–MS/MS to clarify the role of mitochondrial proteins. In a preliminary experiment, however, it was difficult to separate the mitochondrial protein mixture

* Corresponding author. Tel.: +81 42 468 9787; fax: +81 42 468 9787.
E-mail address: k-imai@musashino-u.ac.jp (K. Imai).

0021-9673/$ – see front matter © 2011 Elsevier B.V. All rights reserved.
doi:10.1016/j.chroma.2011.03.070

effectively using the conventional wide-pore column that was used for the FD–LC–MS/MS method. Therefore, we searched for other columns that have higher-performance separation ability than the wide-pore column.

According to recent technical developments, the use of a stationary phase of small and non-porous particles (sub-2 μm) reduces eddy diffusion and mass-transfer resistance in the mobile phase more than porous particles [8]. Chong et al. used sub-2 μm non-porous particles for separating intact proteins in biological samples [9]. However, the reproducibility of the retention time of each protein was very low, probably due to the hydrophobicity of the intact proteins and the large amount of proteins provided for ultraviolet detection, which could prevent using a non-porous column for differential proteomics analysis. In contrast, with FD–LC–MS/MS, the non-porous column seems to be useful because the proteins are derivatized into less hydrophobic ones with the hydrophilic reagent, and one or two orders of magnitude less amount of proteins is sufficient for fluorescence detection than for ultraviolet detection.

Therefore, in this study, we applied a non-porous small-particle reversed-phase column (Presto FF-C18, 2 μm particle, Imtakt) to the FD–LC–MS/MS method. Based on an investigation of column lengths and flow rates for the non-porous column, the optimized FD–LC–MS/MS method was applied to liver mitochondrial proteomics analysis, resulting in high-performance separation of the mitochondrial proteins. This result suggested the non-porous small-particle column as a replacement for the wide-pore column in differential proteomics analysis utilizing the FD–LC–MS/MS method. Also, the result of liver mitochondrial proteomics analysis indicated proteins related to hepatocarcinogenesis; thus, the roles of proteins in hepatocarcinogenesis will be investigated.

2. Experimental

2.1. Reagents

For this study, 7-chloro-N-[2-(dimethylamino)ethyl]-2,1,3-benzoxadiazole-4-sulfonamide (DAABD-Cl) and Buffer Solution pH 8.7 (6 M Guanidine Hydrochloride) were obtained from Tokyo Chemical Industry (Tokyo, Japan). In addition, 3-[(3-cholamidopropyl)dimethylammonio]propanesulfonate (CHAPS) and ethylenediamine-N,N,N′,N′-tetraacetic acid disodium salt (Na_2EDTA) were obtained from Dojindo Laboratories (Kumamoto, Japan). Tris(2-carboxyethyl)phosphine hydrochloride (TCEP) and β-lactoglobulin (M.W. 18,363) were purchased from Sigma–Aldrich (St. Louis, MO, USA). Calcitonin (M.W. 3,418) was purchased from Peptide Institute (Osaka, Japan). Trifluoroacetic acid (TFA) was obtained from Wako Pure Chemical Industries (Osaka, Japan). Acetonitrile (HPLC grade) was obtained from Kanto Chemical (Tokyo, Japan). All the other reagents were of analytical reagent grade and were used without further purification. Water was used after purification with the Milli-Q system (Nihon Millipore, Tokyo, Japan).

2.2. Columns

Non-porous spherical silica (2 μm particle and 2 m^2/g specific surface area) was utilized as packing material in the Presto FF-C18 column (Fig. 1) (Imtakt, Kyoto, Japan). Octadecylsilane (ODS) binds to functional groups on packing materials, indicating that Presto FF-C18 is useful for reversed-phase separation in HPLC. However, wide-pore spherical silica (30 nm pore size, 3 μm particle, and 100 m^2/g specific surface area) was utilized in the Intrada WP-RP column (Imtakt). Reversed-phase ligands exist on the surface of the packing materials of Intrada WP-RP, which was used as a conventional protein separation column for the FD–LC–MS/MS method. Presto FF-C18 columns were adopted with 4.6 mm i.d. and 50–250 mm length, while Intrada WP-RP with 4.6 mm i.d. and 250 mm length was usually utilized for protein separation [2–7].

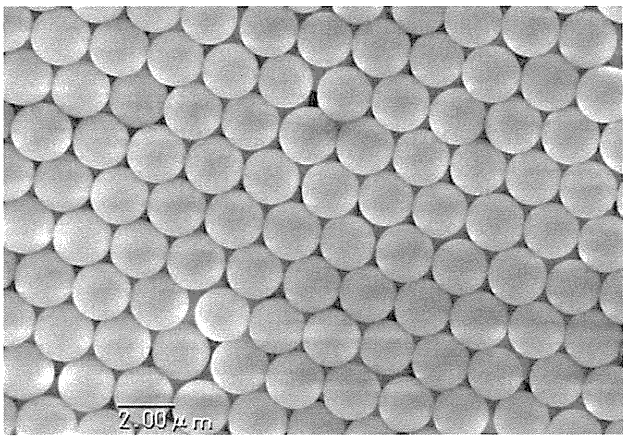

Fig. 1. Electron microscopic image of non-porous spherical silica (2 μm particle) utilized as a packing material in a Presto FF-C18 column.

2.3. FD reaction and separation of DAABD-calcitonin on the non-porous or the wide-pore column

A 10 μL aliquot of 5 μM calcitonin (Peptide Institute, Osaka, Japan) was mixed with 60 μL of 16.7 mM CHAPS/3.33 mM Na_2EDTA/0.833 mM TCEP in 6 M guanidine buffer (pH 8.7), 25 μL of 6 M guanidine buffer (pH 8.7), and 5.0 μL of 140 mM DAABD-Cl in acetonitrile. Each reaction mixture was incubated at 40 °C for 10 min, and the reaction was stopped with 3.0 μL of 20% TFAaq. The reaction mixture was then diluted threefold with the mobile phase. A 10 μL aliquot of the diluted reaction mixture was injected into an HPLC system that consisted of a pump (L-2100, Hitachi) and a fluorescence detector (L-2485, Hitachi). Fluorescence detection was carried out at 505 nm (excitation at 395 nm). Separation was performed on the non-porous column (4.6 i.d. × 50, 100, 150, or 250 mm) or the wide-pore column (4.6 i.d. × 250 mm) (Imtakt, Kyoto, Japan). The column temperature was set at 60 °C, and the flow rate was 0.2–0.5 mL/min. The gradient elution was 10–40% B over 60 min ((A) water:acetonitrile:TFA = 90:10:0.10, v/v/v; (B) water:acetonitrile:TFA = 30:70:0.20, v/v/v).

2.4. Preparation of liver mitochondrial sample and determination of total proteins

Sixteen-month-old Tg and NTg mice were used for analysis. Progression of disease state and morphological features were described in previous reports [4,10].

A preliminary study clearly indicated that an extraction procedure utilizing a mitochondrial isolation commercial kit was not useful, due to the low repeatability in isolation handling. Therefore, in this study, mitochondria were extracted from liver samples (100 mg) by density-gradient centrifugation using a mannitol/sucrose solution, as reported by Lopez et al. [11]. The mitochondrial pellet obtained was suspended with twice-volume of 2% CHAPS in 6 M guanidine buffer (pH 8.7). The suspension was sonicated for 15 s on ice four times at 15 s intervals. The sonicated suspension was centrifuged at 13,000 g for 2 min at 4 °C. The supernatant was then collected and stored as a soluble fraction at −80 °C after freezing with liquid nitrogen. The total liver mitochondrial proteins were determined with a BCA™ Protein Assay

Kit (Thermo Scientific, Rockford, IL, USA), following the written instructions. Bovine serum albumin was used as a protein standard.

2.5. FD–LC–MS/MS method for liver mitochondrial proteomics analysis

The previous method was used for the FD procedure for liver mitochondrial proteins with DAABD-Cl [4], except for the amount of total protein; in brief, 60 μg of liver mitochondrial proteins was derivatized in 100 μL reaction mixture. Twenty microliters of the reaction mixture (12 μg proteins) was subjected to HPLC. Sample proteins amount per injection was low enough as compared to the maximum (24 μg) for separation on the non-porous column. The overall system consisted of a Hitachi L-2000 series HPLC system with a non-porous column (4.6 i.d. × 250 mm) at a column temperature of 60 °C [2] and a flow rate of 0.3 mL/min. Fluorescence detection was carried out at 505 nm (excitation at 395 nm). The compositions of the mobile phases were the same as described above. The 267.5 min gradient program was used to compare the non-porous column with the wide-pore column. The gradient elution was 16% B held over 5 min, to 25% in 10 min, to 43% B in 112.5 min, to 45% B in 135 min, to 55% B in 185 min, to 65% B in 215 min, and to 100% B in 267.5 min. The 535 min gradient program was used for proteomics analysis of mitochondrial proteins in livers of the hepatitis-infected mouse model. The gradient elution was 16% B held over 10 min, to 25% in 20 min, to 43% B in 225 min, to 45% B in 270 min, to 55% B in 370 min, to 65% B in 430 min, and to 100% B in 535 min. To keep the long life-time of the non-porous column, a washing operation was performed after operation of each analysis. The gradient time program of the washing operation was 100 to 0% B in 5 min and 0 to 100% B in 10 min at 0.3 mL/min of flow rate, which was repeated four times.

The isolated derivatized proteins were identified as reported in Ref. [5] using HPLC and tandem mass spectrometry. The obtained amino acids sequence data were searched for the taxonomy *Mus musculus* against the National Center for Biotechnology Information non-redundant (NCBInr) database using MASCOT version 2.1.03 (Matrix Science, Ltd., London, UK).

3. Result

3.1. Separation of DAABD-calcitonin in gradient elution with the non-porous column

The non-porous column was applied to separate fluorogenic derivatized calcitonin, a model peptide, to investigate its separation efficiency. Calcitonin (0.5 μM, M.W. 3418) was derivatized with a fluorogenic reagent, 7.0 mM DAABD-Cl, and subjected to HPLC-fluorescence detection in gradient elution on either the non-porous or the wide-pore column. Both columns were the same size (4.6 i.d. × 250 mm). The retention times and shapes of both DAABD-calcitonin peaks suggested that the non-porous column exhibited stronger affinity for the peptide and higher resolution than the wide-pore column (Fig. 2). The retention time of the compounds less retained on the non-porous column was shorter than that on the wide-pore column. The separation efficiencies of both columns were then compared utilizing the peak capacity, since the separation efficiency of HPLC columns in gradient elution is usually evaluated with column peak capacity P, while under isocratic conditions it is evaluated with theoretical plates N. The peak capacity represents the maximum theoretical number of components that can be separated in a column within a given gradient time. Each P value was then calculated from peak width w measured at 4σ

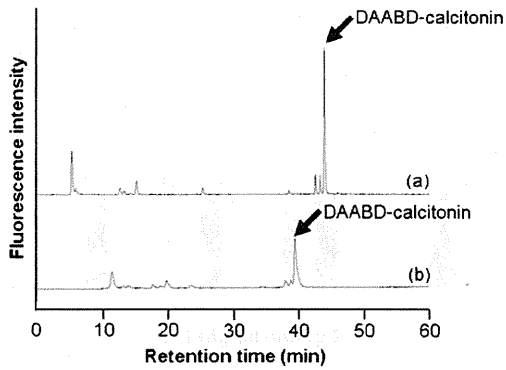

Fig. 2. Chromatograms obtained from DAABD-calcitonin separated in (a) the non-porous column or (b) the wide-pore column under gradient elution conditions. Chromatographic conditions are described in Section 2.

(13.4% of peak height) and the gradient time t_g according to Eq. (1) [12]:

$$P = 1 + \frac{t_g}{w} \quad (1)$$

The P value with the non-porous column was found to be three-fold higher than that with the wide-pore column under 60 min gradient conditions (197 with the non-porous column vs. 64 with the wide-pore column). In a similar experiment using a typical standard protein (β-lactoglobulin, M.W. 18,363), the P value exhibited the same tendency with both columns (data not shown). These results indicate that separation efficiency in the non-porous column was superior to that in the wide-pore column.

3.2. Optimized column length and flow rate with the non-porous column

In order to obtain appropriate separation efficiency, the gradient elution of DAABD-calcitonin was performed with different lengths (50, 100, 150, and 250 mm) of the non-porous column at different flow rates (0.2, 0.3, 0.4, and 0.5 mL/min). However, for the 250 mm-long column, the flow rate was limited to a maximum of 0.3 mL/min because of the durability of the HPLC flow (20 MPa) system used in the present experiment. DAABD-calcitonin was separated in the same 60 min gradient program as described in Section 3.1, and each P value was calculated according to Eq. (1). The P value increased with increasing column length and flow rate, indicating that separation efficiency was greater with a longer column and a higher flow rate (Fig. 3A). The same was true for β-lactoglobulin, a model protein (data not shown).

Moreover, mitochondrial protein extract was injected into each length of the columns at the maximum flow rate (0.3 or 0.5 mL/min) to investigate the separation of a real biological sample. The number of separated protein peaks increased with increasing column length: a 250 mm-long column at a 0.3 mL/min flow rate exhibited the highest separation efficiency for the actual protein mixture sample (Fig. 3B). Therefore, a column length of 250 mm with a flow rate of 0.3 mL/min was selected for separating the mitochondrial protein extract.

3.3. Comparison of the non-porous column with the wide-pore column for separating a mitochondrial protein extract

Based on the results above, the non-porous column (250 mm length with a flow rate of 0.3 mL/min) was applied to separate a mitochondrial protein extract. The chromatogram obtained under the appropriate conditions described in Section 2.5 was compared with that obtained from the wide-pore column (250 mm length,

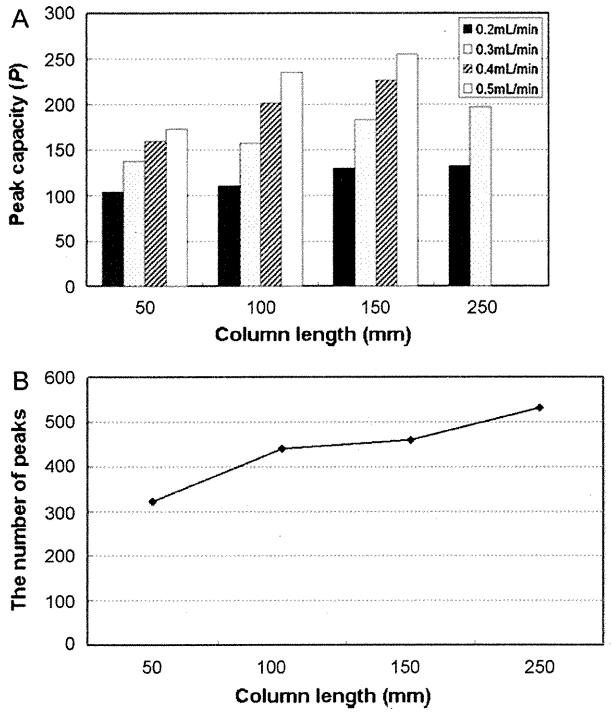

Fig. 3. (A) Peak capacities of the non-porous column with various column lengths (50, 100, 150, and 250 mm) at various flow rates (0.2, 0.3, 0.4, and 0.5 mL/min) in the gradient elution of DAABD-calcitonin. Each *P* value was calculated with Eq. (1) in Section 3.2. (B) The number of protein peaks separated in each length of the column (50, 100, 150, and 250 mm) obtained from the mitochondrial protein extract. The flow rate was 0.5 mL/min, except for the 250 mm column that had a 0.3 mL/min flow rate. The details are described in Section 2.

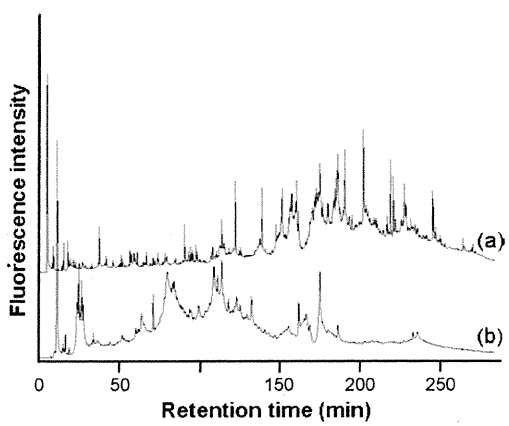

Fig. 4. Chromatograms of mouse liver mitochondrial proteins separated in (a) the non-porous column or (b) the wide-pore column. Chromatographic conditions are described in Section 2.

0.3 mL/min). Fig. 4a indicates that 420 protein peaks were obtained on the chromatogram with the non-porous column in 260 min analytical time. However, 160 protein peaks were not clearly separated in the chromatogram with the wide-pore column (Fig. 4b). This result clearly suggested that the non-porous column, rather than the wide-pore column, would be useful for proteomics analysis of mouse liver mitochondrial proteins with the FD–LC–MS/MS method.

Also, the retention times and peak shapes of the proteins injected into the non-porous column exhibited stronger adsorption and higher resolution than those injected into the wide-pore column. Furthermore, the retention time of the compounds less

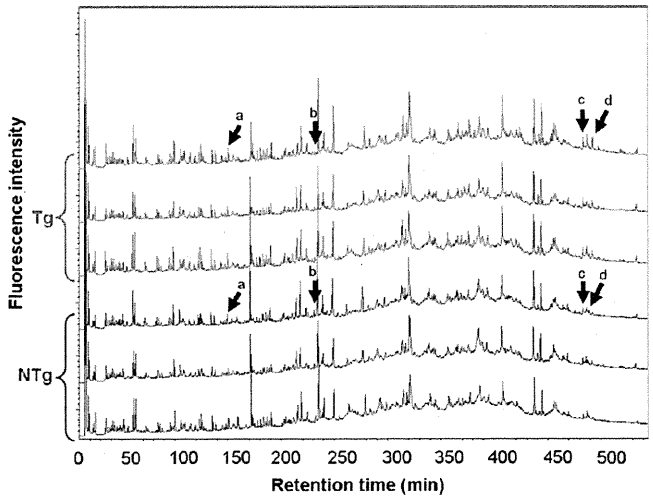

Fig. 5. Chromatograms of liver mitochondrial proteins in Tgs (red) and NTgs (blue) mice separated in the non-porous column. The peaks indicated by arrows fluctuated between Tgs and NTgs. Chromatographic conditions are described in Section 2. (For interpretation of the references to color in this figure legend, the reader is referred to the web version of the article.)

retained in the non-porous column was shorter than that on the wide-pore column.

3.4. Proteomics analysis of mitochondrial proteins in livers of hepatitis-infected mouse model

Differential proteomics analysis was performed on the non-porous column between mitochondrial protein samples extracted from livers of Tgs ($n=3$) and NTgs ($n=3$) mice aged 16 months. This age was selected based on the previous report that many proteins related to the function of mitochondrial events fluctuated in Tg. The appropriate separation conditions in HPLC afforded 500 protein peaks on each chromatogram for Tgs and NTgs in 9 h of analysis (Fig. 5), with each peak height representing the amount of each protein. The responsibility of this analysis was confirmed, based on the reproducibility of the retention times and the peak heights. The relative standard deviations (RSDs) of peaks a through d (Fig. 5) ranged from 0.0 to 0.5% for retention times and 0.4–18.0% for peak heights (for between-days, $n=3$–6). The heights of peaks corresponding to specific retention times were compared between Tgs and NTgs. The expression of several peaks fluctuated, and each fluctuating peak fraction was collected, digested, and subjected to LC–MS/MS analysis to identify the protein. Table 1 summarizes the identified proteins. Three proteins were significantly up-regulated (Tg/NTg = 1.24–2.86, $0.05 \leq p < 0.10$) (Peaks a, c, and d in Fig. 5) in Tg, while one protein peak was significantly down-regulated (Tg/NTg = 0.44, $p < 0.05$) (Peak b in Fig. 5). Those four proteins were demonstrated for the first time in liver mitochondrial proteomics analysis.

4. Discussion

4.1. Comparison of the separation of DAABD-calcitonin and DAABD-β-lactoglobulin between the non-porous column and the wide-pore column

In order to determine the difference in separation between the non-porous column and the wide-pore column, a derivatized model peptide and protein (DAABD-calcitonin and DAABD-β-lactoglobulin) were separated. The retention times of the derivatized model samples were longer for the non-porous col-

Table 1
Differentially expressed liver mitochondrial proteins between Tgs and NTgs.

Peak number	Tg/NTg ratio		Protein name	Accession number	Score	Sequence coverage (%)
a	1.24	± 0.17	60S ribosomal protein L11	gi 13385408	129	12
b	0.44	± 0.33	Sterol-carrier protein 2	gi 45476581	278	10
c	1.51	± 0.35	NADH-cytochrome b5 reductase 3	gi 19745150	145	8
d	2.86	± 1.30	Hydroxysteroid (17-beta) dehydrogenase 13	gi 159573879	183	25

umn than for the wide-pore column. Since the surface of the non-porous column is covered with ODS (C18) and the surface of the wide-pore column consists of a less hydrophobic "reversed-phase" ligand than C18, stronger retention of the derivatized model samples should be caused by the hydrophobic interaction in the non-porous column. In contrast, considering the shortest retention times of the hydrophilic substances, the non-porous column should exhibit fewer void volumes than the wide-pore column. It was also shown that, considering the *P* (peak capacity) value for the non-porous column was threefold higher than that for the wide-pore column, the non-porous and small size (2 μm as compared to 3 μm of the wide-pore column) reduced eddy diffusion and mass-transfer resistance on separation and resulted in high-resolution chromatography [8]. This couldn't be caused by the narrow particle size distribution of the former column since the particle size distribution of both the columns were similar (D90/D10 < 1.4, and D90/D10 = 1.42 for the non-porous and the wide-pore, respectively, measured by laser diffraction particle size analysis and electrical sensing zone method).

4.2. Optimization of column length and flow rate for protein separation with the non-porous column

The effects of column length and flow rate on the *P* value were investigated using DAABD-calcitonin and DAABD-β-lactoglobulin to obtain optimal conditions for derivatized protein separation on the non-porous column. High *P* values were obtained using a longer column and a higher flow rate. This tendency agreed with the simulation of separation efficiency reported by Gilar et al. [12], indicating that the length of the non-porous column was proportional to separation efficiency. In this study, 0.3 mL/min was the maximum flow rate for the longest column (250 mm) because of the currently limited operating pressure (20 MPa). The LC system should be mechanically strong enough to withstand the ultrahigh pressures for further efficient separation in the non-porous Presto FF-C18 that might be 250 mm long and have a flow rate exceeding 0.3 mL/min. In this sense, in the future, further efficient separation should be examined utilizing an Ultra High Pressure Liquid Chromatography system. According to the results (Fig. 3A), the highest *P* value was obtained with a 150 mm length of column and a flow rate of 0.5 mL/min. However, more separated proteins were observed in the 250 mm-long column with a 0.3 mL/min flow rate for the mitochondrial sample (Fig. 3B). This is because the separable peaks from a large numbers of proteins in a real biological sample should be proportional to the column length. Another reason is that the dilution of the peak fraction in a 150 mm column with a high flow rate of 0.5 mL/min might be beyond the detection limit of the system. Therefore, a 250 mm column length with a flow rate of 0.3 mL/min was adopted as the optimal condition for separating liver mitochondrial proteins.

4.3. Application of the FD–LC–MS/MS method using the non-porous column for differential proteomics analysis of liver mitochondria

Nine hours of analysis indicated that the number (500) of mitochondrial protein peaks (Fig. 5) was similar to the number of extracted proteins from a whole cell separated with the wide-pore column (e.g., for mouse liver proteomics analysis) [4]. Concerning the life-time of the non-porous column, the life-time was long enough to analyze mitochondrial proteins about 40 times (400 h including the washing period) since the chromatogram obtained after 40 times analyses was the same as the initial one. That would be caused by the contribution of a washing operation after each analysis. This result suggests that the non-porous column could be substituted for the wide-pore column as a protein separation column for the FD–LC–MS/MS method.

Compared to the low reproducibility for the retention times of peaks in the previous report [9], the present differential proteomics analysis of liver mitochondria obtained reproducible retention times and peak heights (RSD less than 0.5% for retention times and less than 18.0% for peak heights). The reason for this superior reproducibility may be that in the FD–LC–MS/MS method, proteins were derivatized with the hydrophilic reagent and a low amount of proteins. These results indicate that the FD–LC–MS/MS method using the non-porous column can be used for differential proteomics analysis of liver mitochondria and results in identification of four fluctuating proteins between Tgs and NTgs.

4.4. Functions of the fluctuating liver mitochondrial proteins related to hepatocarcinogenesis

All the identified mitochondrial proteins in this study were demonstrated for the first time in liver proteomics analysis. Since mitochondria were extracted from mouse liver and analyzed for expression of proteins, it is assumed that the proteins inside the mitochondria were concentrated to a detectable level of each expression fluctuation.

Only one down-regulated peak in Tg was identified as sterol carrier protein 2 (SCP2), considering differences in localization between the deduced different types (SCP2 and SCPx) (reviewed in ref. [13]). SCP2 is related to intracellular lipid transport (e.g., cholesterol) from other intracellular membranes to mitochondria [14], as well as from the outer to the inner mitochondrial membrane for oxidation. Since lipids have accumulated in the hepatocytes of 16-month-old Tg mice, causing steatosis as previously reported [10], lipid transport to mitochondria might no longer be required. Thus, SCP2 was decreased in Tg through a negative feedback pathway. Also, SCP2 is reportedly involved in regulation of the signal pathway for lipids (reviewed in ref. [13]). These findings suggest that the decrease of SCP2 in Tg may suppress lipid transport to mitochondria, leading to inhibition of lipid signaling. In contrast, three proteins were demonstrated to be up-regulated in Tg. Hydroxysteroid (17-beta) dehydrogenase 13 (17βHSD13) is specifically expressed in liver [15]. It has been reported that the intracellular localization of 17βHSD13 is similar to that of HCV core protein in endoplasmic reticulum (ER), lipid droplets (LDs), and mitochondria [16–18], while it is unknown whether 17βHSD13 localizes in mitochondria or not. In general, 17βHSD family proteins catalyze the dehydrogenation reactions of the steroid skeleton with an excess of NADH or electrons. Although 17βHSD13 may play a key role in the next step of detoxification and/or utilization of lipid metabolites through the reaction, its specific substrate is not identified. At least, the increase of 17βHSD13 in Tgs would acti-

vate lipid metabolism. NADH-cytochrome b5 reductase 3 (CYB5R3) was observed in the plasma membrane, mitochondrial outer membrane, and ER. CYB5R3 in the mitochondrial electron-transfer system catalyzes the oxidation of NADH to NAD^+ (reviewed in Ref. [19]). For mitochondrial dysfunction, CYB5R3 is up-regulated due to an increase of the NADH/NAD^+ ratio, resulting in enhanced oxidation of NADH to NAD^+. Thus, an increase of CYB5R3 in Tg would accelerate aerobic respiration in mitochondria. In addition, 60S ribosomal protein L11 (RPL11) is associated with Mdm2, which is an E3 ligase for promoting p53 ubiquitination, resulting in prevention of the degradation of p53 [20,21]. The undegraded p53 in mitochondria reportedly causes apoptosis of cancer cells [22,23]. This finding suggests that up-regulated RPL11 would suppress the growth of hepatocarcinoma in transition out of hepatitis C. If hepatocarcinogenesis activates metabolism in Tg mice at the age of 16 months, 17βHSD13 and CYB5R3 might increase and accelerate lipid metabolism and aerobic respiration. Furthermore, a decrease of SCP2 might control lipid transport to mitochondria and thus maintain equilibrium through a negative feedback pathway. Considering these results, fluctuation of these proteins suggests that activation and suppression of hepatocarcinogenesis occur simultaneously in Tg mice at 16 months of age.

In conclusion, a novel non-porous column (Presto FF-C18) achieved good separation of liver mitochondrial proteins, which was hardly achieved on a wide-pore column such as Intrada WP-RP. Moreover, the FD–LC–MS/MS method with Presto FF-C18 demonstrated for the first time several fluctuating proteins performing differential proteomics analysis of liver mitochondrial proteins in a hepatitis-infected mouse model.

References

[1] H.J. Issaq, J. Blonder (Eds.), J. Chromatogr. B: Analyt. Technol. Biomed. Life Sci. Netherlands (2009) 1222.
[2] M. Masuda, H. Saimaru, N. Takamura, K. Imai, Biomed. Chromatogr. 19 (2005) 556.
[3] T. Ichibangase, H. Saimaru, N. Takamura, T. Kuwahara, A. Koyama, T. Iwatsubo, K. Imai, Biomed. Chromatogr. 22 (2008) 232.
[4] T. Ichibangase, K. Moriya, K. Koike, K. Imai, J. Proteome Res. 6 (2007) 2841.
[5] K. Imai, T. Ichibangase, R. Saitoh, Y. Hoshikawa, Biomed. Chromatogr. 22 (2008) 1304.
[6] H. Asamoto, T. Ichibangase, K. Uchikura, K. Imai, J. Chromatogr. A 1208 (2008) 147.
[7] T. Ichibangase, K. Imai, J. Proteome Res. 8 (2009) 2129.
[8] N. Wu, Y. Liu, M.L. Lee, J Chromatogr A, Netherlands (2006) 142.
[9] B.E. Chong, D.M. Lubman, F.R. Miller, A.J. Rosenspire, Rapid Commun. Mass Spectrom. 13 (1999) 1808.
[10] K. Moriya, H. Yotsuyanagi, Y. Shintani, H. Fujie, K. Ishibashi, Y. Matsuura, T. Miyamura, K. Koike, J. Gen. Virol. 78 (Pt 7) (1997) 1527.
[11] M.F. Lopez, B.S. Kristal, E. Chernokalskaya, A. Lazarev, A.I. Shestopalov, A. Bogdanova, M. Robinson, Electrophoresis 21 (2000) 3427.
[12] M. Gilar, A.E. Daly, M. Kele, U.D. Neue, J.C. Gebler, J. Chromatogr. A 1061 (2004) 183.
[13] F. Schroeder, B.P. Atshaves, A.L. McIntosh, A.M. Gallegos, S.M. Storey, R.D. Parr, J.R. Jefferson, J.M. Ball, A.B. Kier, Biochimica Et Biophysica Acta-Mol. Cell Biol. Lipids 1771 (2007) 700.
[14] G.G. Martin, H.A. Hostetler, A.L. McIntosh, S.E. Tichy, B.J. Williams, D.H. Russell, J.M. Berg, T.A. Spencer, J. Ball, A.B. Kier, F. Schroeder, Biochemistry 47 (2008) 5915.
[15] Y. Horiguchi, M. Araki, K. Motojima, Biochem. Biophys. Res. Commun. 370 (2008) 235.
[16] K. Moriya, H. Fujie, Y. Shintani, H. Yotsuyanagi, T. Tsutsumi, K. Ishibashi, Y. Matsuura, S. Kimura, T. Miyamura, K. Koike, Nat. Med. 4 (1998) 1065.
[17] R. Suzuki, S. Sakamoto, T. Tsutsumi, A. Rikimaru, K. Tanaka, T. Shimoike, K. Moriishi, T. Iwasaki, K. Mizumoto, Y. Matsuura, T. Miyamura, T. Suzuki, J. Virol. 79 (2005) 1271.
[18] B. Schwer, S.T. Ren, T. Pietschmann, J. Kartenbeck, K. Kaehlcke, R. Bartenschlager, T.S.B. Yen, M. Ott, J. Virol. 78 (2004) 7958.
[19] R. de Cabo, E. Siendones, R. Minor, P. Navas, Aging (Albany NY) 2 (2010) 63.
[20] K. Itahana, H. Mao, A.W. Jin, Y. Itahana, H.V. Clegg, M.S. Lindstrom, K.P. Bhat, V.L. Godfrey, G.I. Evan, Y.P. Zhang, Cancer Cell 12 (2007) 355.
[21] S. Fumagalli, A. Di Cara, A. Neb-Gulati, F. Natt, S. Schwemberger, J. Hall, G.F. Babcock, R. Bernardi, P.P. Pandolfi, G. Thomas, Nat. Cell Biol. 11 (2009) 501.
[22] N.D. Marchenko, A. Zaika, U.M. Moll, J. Biol. Chem. 275 (2000) 16202.
[23] M. Mihara, S. Erster, A. Zaika, O. Petrenko, T. Chittenden, P. Pancoska, U.M. Moll, Mol. Cell 11 (2003) 577.

Research Article

EASL EUROPEAN ASSOCIATION FOR THE STUDY OF THE LIVER | JOURNAL OF HEPATOLOGY

Altered composition of fatty acids exacerbates hepatotumorigenesis during activation of the phosphatidylinositol 3-kinase pathway

Yotaro Kudo[1], Yasuo Tanaka[1], Keisuke Tateishi[1,*], Keisuke Yamamoto[1], Shinzo Yamamoto[1], Dai Mohri[1], Yoshihiro Isomura[1], Motoko Seto[1], Hayato Nakagawa[1], Yoshinari Asaoka[1], Motohisa Tada[2], Miki Ohta[1], Hideaki Ijichi[1], Yoshihiro Hirata[1], Motoyuki Otsuka[1], Tsuneo Ikenoue[1], Shin Maeda[3], Shuichiro Shiina[1], Haruhiko Yoshida[1], Osamu Nakajima[4], Fumihiko Kanai[2], Masao Omata[5], Kazuhiko Koike[1]

[1]*Department of Gastroenterology, Graduate School of Medicine, The University of Tokyo, 7-3-1 Hongo, Bunkyo-ku, Tokyo 113-8655, Japan;* [2]*Department of Medicine and Clinical Oncology, Graduate School of Medicine, Chiba University, 1-8-1 Inohana, Chuo-ku, Chiba-shi, Chiba 260-8670, Japan;* [3]*Department of Gas troenterology, Yokohama City University, Graduate School of Medicine, 3-9 Fuku-ura, Kanazawa-ku, Yokohama 236-0004, Japan;* [4]*Research Laboratory for Molecular Genetics, Yamagata University, Yamagata 990-9585, Japan;* [5]*Yamanashi Prefectural Central Hospital, 1-1-1 Fujimi, Kofu-shi, Yamanashi 400-8506, Japan*

Background & Aims: Some clinical findings have suggested that systemic metabolic disorders accelerate *in vivo* tumor progression. Deregulation of the phosphatidylinositol 3-kinase (PI3K)/Akt pathway is implicated in both metabolic dysfunction and carcinogenesis in humans; however, it remains unknown whether the altered metabolic status caused by abnormal activation of the pathway is linked to the protumorigenic effect.

Methods: We established hepatocyte-specific *Pik3ca* transgenic (Tg) mice harboring N1068fs*4 mutation.

Results: The Tg mice exhibited hepatic steatosis and tumor development. PPARγ-dependent lipogenesis was accelerated in the Tg liver, and the abnormal profile of accumulated fatty acid (FA) composition was observed in the tumors of Tg livers. In addition, the Akt/mTOR pathway was highly activated in the tumors, and in turn, the expression of tumor suppressor genes including *Pten*, *Xpo4*, and *Dlc1* decreased. Interestingly, we found that the suppression of those genes and the enhanced *in vitro* colony formation were induced in the immortalized hepatocytes by the treatment with oleic acid (OA), which is one of the FAs that accumulated in tumors.

Conclusions: Our data suggest that the unusual FA accumulation has a possible role in promoting *in vivo* hepato-tumorigenesis under constitutive activation of the PI3K pathway. The *Pik3ca* Tg mice might help to elucidate molecular mechanisms by which metabolic dysfunction contributes to *in vivo* tumor progression.
© 2011 European Association for the Study of the Liver. Published by Elsevier B.V. All rights reserved.

Introduction

Accumulating clinical evidence suggests that systemic metabolic disorders including obesity and insulin resistance can affect or even promote *in vivo* tumor progression [1–4]. Some studies have outlined the impact of fat-enriched diets in the development of hepatocellular carcinoma (HCC) [5–7]. However, the mechanistic insights regarding metabolites or cellular signaling responsible for the development of HCC in altered metabolic states remain unknown.

The phosphatidylinositol 3-kinase (PI3K)/Akt signaling pathway is involved in various cellular processes including cell metabolism, growth, and survival [8,9]. The altered expression and mutation of PI3K/Akt-related signaling components have been detected in some human cancers [10]. In particular, the *PIK3CA* gene encoding p110α, which is a catalytic subunit of PI3K, has somatic mutations in some carcinomas [11]. Additionally, a mutation in its kinase domain has been reported in HCC and gastric cancer [12]. These findings indicate that deregulated PI3K activity plays certain roles in oncogenesis in humans [11,13]. PI3K signaling is antagonized by phosphatase and tensin homolog deleted on chromosome 10 (PTEN) phosphatase [14]. The expression of PTEN is decreased or absent in approximately half of HCC patients [15], and hepatocyte-specific *Pten* knockout

Keywords: Hepatocellular carcinoma; Fatty acids; NAFLD; Tumor suppressor genes.
Received 3 October 2010; received in revised form 25 March 2011; accepted 27 March 2011; available online 19 May 2011
*Corresponding author. Tel.: +81 3 3815 5411x33070; fax: +81 3 3814 0021.
E-mail address: ktate-tky@umin.ac.jp (K. Tateishi).
Abbreviations: PI3K, phosphatidylinositol 3-kinase; Tg, transgenic; FA, fatty acid; OA, oleic acid; HCC, hepatocellular carcinoma; PTEN, phosphatase and tensin homolog deleted on chromosome 10; FBS, fetal bovine serum; Erk, extracellular signal-regulated kinase; WT, wild type; PA, palmitic acid; H&E, hematoxylin and eosin; NASH, non-alcoholic steatohepatitis.

mice develop steatohepatitis and HCC [16]. These findings indicate that PTEN is a tumor suppressor in the liver [17]. Although recent reports have suggested unique functions of PTEN that are independent of the PI3K-Akt axis [18–20], it is unknown whether the phenotype in *Pten*-deficient mice is due to PI3K-dependent or PI3K-independent processes.

To address the pathological consequences caused by the abnormal activation of PI3K pathway *in vivo*, we generated liver-specific *Pik3ca* transgenic (Tg) mice. In this study, we proposed that abnormal fat composition, as observed in the *Pik3ca* Tg liver, is a mechanism by which metabolic deregulation is linked to *in vivo* tumor progression.

Materials and methods

Generation of Pik3ca Tg mice

The *Pik3ca* Tg mice were generated as described previously [21]. Briefly, Myc-tagged mouse *Pik3ca* cDNA (N1068fs*4) was cloned into the p2335A-1 vector (provided by Drs. Palmiter and Chisari) [22,23]. The microinjection was conducted by the Research Laboratory for Molecular Genetics, Yamagata University. Founder BDF1 mice (F0) were backcrossed with C57BL/6JJcl mice (CLEA Japan, Japan), and F5 mice were analyzed. The primers for genotyping were 5′-ATGGAACAGAAACTCATCTCT-3′ and 5′-GGGTGACACTTACGAAAAT-3′. All procedures involving animals were performed in accordance with protocols approved by the institutional committee for animal research at the University of Tokyo and complied with the Guide for the Care and Use of Laboratory Animals.

Cell cultures, viruses, and treatment with fatty acids

Lentiviral short hairpin RNA vectors were purchased from Open Biosystems (Huntsville, AL, USA). BNL-CL2 cells were infected with the virus according to the manufacturer's protocol and selected by puromycin. BNL-CL2 cells were incubated with either 50 μmol/L fatty acids or ethanol (mock) for 12 h in the absence of fetal bovine serum (FBS) in some experiments.

Antibodies and primers

The primers for quantitative RT-PCR are shown in Supplementary Table 1. Antibodies against phospho-Akt (Ser473 and Thr308), Akt, phospho-extracellular signal-regulated kinase (Erk) 1/2 (Thr202/Tyr204), Erk1/2, phospho-TSC2, phospho-S6K, TSC2, S6K, and SREBP1 were obtained from Cell Signaling Technology (Danvers, MA, USA). The anti-PTEN antibody was purchased from Neomarkers Inc. (Frement, CA, USA). The anti-TFIID antibody was purchased from Upstate Biotechnology Inc. (Lake Placid, NY, USA). For immunohistochemistry, the anti-phospho-Akt (Ser473) antibody and anti-Myc antibodies (Cell Signaling Technology) were used. The immunoblot data were quantified using Multi Gauge ver. 3.1 software (Fuji Film Corp., Tokyo, Japan).

Triacylglycerol content, serum alanine aminotransferase (ALT) levels, and FA composition

Triacylglycerols were extracted from the liver with chloroform–methanol (2:1, v/v), and the levels were determined by the GK-GPO method (Wako, Tokyo, Japan). Serum samples for ALT measurement were collected after a 16-h starvation (SRL, Tokyo, Japan). Fatty acids were extracted from frozen liver samples, and the composition was analyzed by gas chromatography (Kotobiken Medical Laboratories, Inc., Tokyo, Japan).

Glucose tolerance tests

Glucose was intraperitoneally injected into 8-week-old mice fasting for 16 h (1.5 mg of glucose/g body weight). Glucose concentration was measured using the FreeStyle FREEDOM Blood Glucose Monitoring System (Nipro, Tokyo, Japan) at 0, 15, 30, 60, 90, and 120 min after injection.

Oxidative stress evaluation

The measurement of hydrogen peroxide concentrations was performed by the Colorimetric Hydrogen Peroxide Kit (Assay Designs, Inc., Ann Arbor, MI, USA). Thiobarbituric acid reactive substances (TBARS) were measured by the TBARS Assay Kit (ZeptoMetrix, Buffalo, NY, USA).

Immunohistochemistry

Antigen retrieval on paraffin sections was performed by the acetylation method. Proteins were visualized using the standard 3,3′-diaminobenzidine protocol.

Soft agar assay

The lower layer of 0.5% agar in media was placed in a 35-mm dish. Cells (2.5×10^4) were suspended in the upper layer of 0.3% agar. Colonies (>25 μm in diameter) were counted after 14 days. Oleic acid (OA) (50 μmol/L) or ethanol was added to the upper layer in some experiments.

Statistics

All results are indicated as means ± SE. Statistics were performed by Student's *t*-test or ANOVA followed by Fisher's PLSD host-hoc test. *p*-Values <0.05 were considered statistically significant.

Results

Generation of hepatocyte-specific Pik3ca Tg mice

We established 2 independent lines of hepatocyte-specific Tg mice (*Pik3ca* Tg mice) harboring an "N1068fs*4" mutation in the kinase domain [12]. Myc-tagged mutant *Pik3ca* was designed to be expressed under the albumin promoter (Supplementary Fig. 1), and the liver-specific expression of the transgene was confirmed as shown in Fig. 1A. To assess the *in vivo* effect of the *Pik3ca* N1068fs*4 transgene, we analyzed the activity of molecules downstream of PIK3CA including Akt, TSC2, and S6K via immunoblotting. The phosphorylation of Akt, TSC2, and S6K was clearly increased both in the two lines of Tg livers, but not in the wild-type (WT) livers (Fig. 1B).

Constitutive activation of Pik3ca leads to fat accumulation in the liver

Both lines of *Pik3ca* Tg mice survived, and no difference in total body weight was observed between *Pik3ca* Tg and WT mice at 4 or 24 weeks of age (data not shown). The *Pik3ca* Tg2 mice exhibited better glucose tolerance than WT mice at 8 weeks (Supplementary Fig. 2). The ratio of liver weight to body weight was significantly increased in the *Pik3ca* Tg mice compared to that of WT mice (Fig. 2A). The livers of 4 week-old *Pik3ca* Tg mice appeared slightly enlarged and light-colored, and they exhibited obvious fatty changes by 24 weeks (Fig. 2B). The Tg livers contained a greater volume of triacylglycerol than WT (Fig. 2C). The results of Western blotting revealed that Tg2 mice exhibited a relatively low activation of Akt and S6K as compared to Tg1 (Fig. 1B); however, hepatic triacylglycerol levels were clearly increased in the two lines Tg mice (Fig. 2C). Indeed, even Tg2 mice demonstrated an obvious fatty change in their livers by 24 weeks (Fig. 2B and D). These findings indicated that the constitutive expression of the *Pik3ca* N1068fs*4 transgene has a potential to establish *in vivo* hepatic steatosis. In addition, we found

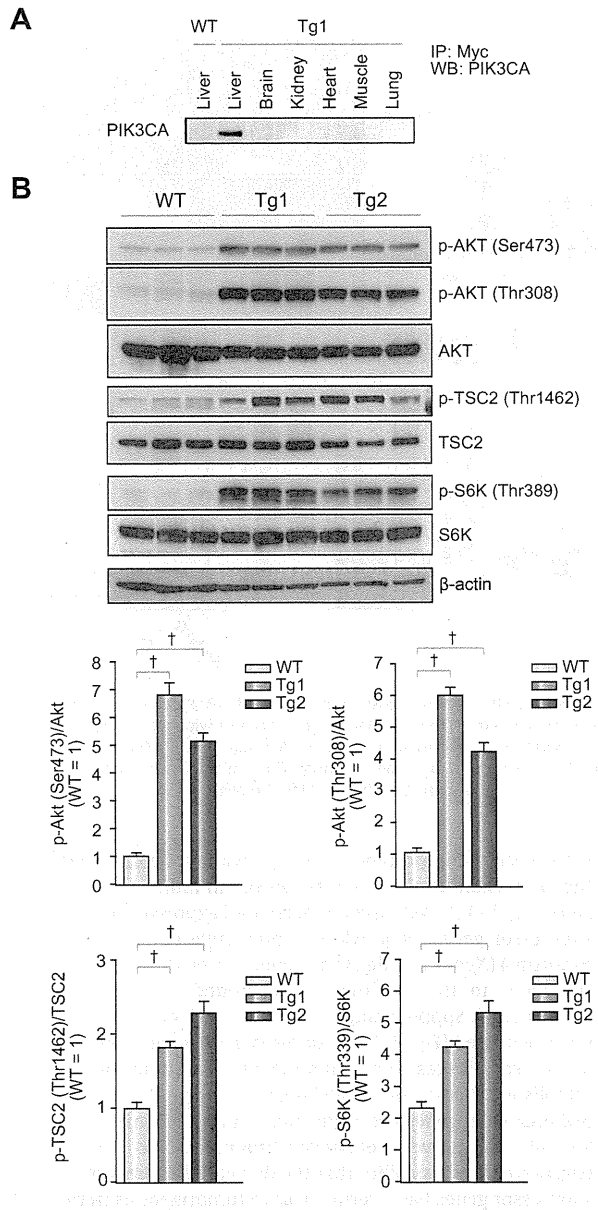

Fig. 1. Establishment of *Pik3ca* Tg mice. (A) Liver-specific expression of the mutant PIK3CA (N1068fs*4). (B) Immunoblots and quantification of the ratios of phosphorylated-Akt, TSC2, and S6K levels to total protein levels (†p <0.05, ANOVA; post hoc test with WT).

that ALT levels in the *Pik3ca* Tg mice were higher than those of WT mice (Fig. 2E), suggesting the coexistence of liver damage. Next, we examined how the *Pik3ca* Tg liver induced unusual lipid accumulation. Because lipogenesis is mainly mediated by two major transcription factors, PPARγ and SREBP1C [24,25], we measured their expression levels and their target genes in Tg2 mice livers and observed the upregulation of PPARγ and its target aP2 but not of SREBP1C or its target FASN (Fig. 2F). Given the previous finding that activated PI3K signaling can induce steatosis through PPARγ [26], we speculated that PPARγ-dependent lipogenesis is a process responsible for hepatic steatosis in Tg mice. This was supported by the finding that the nuclear accumulation of the active form of SREBP1c protein was not increased by *Pik3ca* (N1068fs*4) expression (Supplementary Fig. 3). To emphasize this notion, we investigated whether the *in vitro* overexpression of *Pik3ca* (N1068fs*4) induced lipid accumulation and the activation of PPARγ-dependent transcription. The *in vitro* overexpression of *Pik3ca* (N1068fs*4) increased the concentration of triacylglycerol in BNL-CL2 cells, immortalized normal hepatocytes derived from a BALB/c mouse [27] (Fig. 2G), and upregulated *aP2* expression (Fig. 2H). These data indicated that the overexpression of *Pik3ca* (N1068fs*4) directly contributes to the enhanced lipogenesis, at least via activating PPARγ-dependent transcription. Given the important role of mTOR in lipogenesis through PPARγ, there is a possibility that the activation of mTOR signaling (Fig. 1B) contributes to deregulated lipogenesis through PPARγ signaling in the *Pik3ca* Tg liver [26].

Tumor formation without inflammation in the Pik3ca Tg mice

Regardless of the marked fatty changes and suggested liver damage, *Pik3ca* Tg livers did not exhibit cellular infiltration or fibrotic change even at 52 weeks of age (Fig. 3A and B), which means the expression of the *Pik3ca* transgene is not sufficient for progression to steatohepatitis in the mouse liver. We found that the inflammatory cytokine IL-1α and Fas ligand were highly expressed in the *Pik3ca* Tg liver than WT (Supplementary Fig. 4). Given the previous findings that these factors can be responsible for liver damage [28,29], the abnormal upregulation of IL-1α and Fas ligand in Tg livers may explain a part of the mechanisms of liver damage, whereas the entire molecular process inducing them remains unknown. Notably, macroscopic hepatic tumors developed in 94% of Tg1 mice (30/32) and 100% of Tg2 mice (11/11) at 52 weeks of age (Fig. 3C, left). Most of the tumors were hepatocellular adenomas containing abundant lipid droplets (Fig. 3C, right). Some tumors had rough surfaces and irregular shapes with necrosis and hemorrhaging (Fig. 3D, left) and microscopically demonstrated characteristics of HCC such as enlarged and hyperchromatic nuclei and trabecular patterns (Fig. 3D, right). HCC tissues did not always exhibit lipid accumulation as shown in Fig. 3D. As the *Pik3ca* Tg mice aged, hepatic tumors became increased in number and size, whereas no WT littermates developed any tumors (Fig. 3E). These data clearly indicate that the *in vivo* constitutive expression of *Pik3ca* (N1068fs*4) leads to hepatic tumor development. To assess the functional activity of PIK3CA (N1068fs*4) for tumorigenesis, we examined the *in vitro* transforming ability using BNL-CL2 cells. Remarkably, *Pik3ca* (N1068fs*4) expression did not stimulate colony formation of BNL-CL2 cells (Supplementary Fig. 5). In addition, we analyzed the phosphorylation level of Akt by the *in vitro* overexpression of *Pik3ca* genes including wild type, H1047R, or N1068fs*4 in 293T cells. The overexpression of *Pik3ca* (H1047R) possessing *in vitro* transforming capacity [13] resulted in strong phosphorylation of Akt, as previously reported (Supplementary Fig. 6) [30]. Conversely, the overexpression of *Pik3ca* (wild type) without any transforming capacity [13] resulted in lower phosphorylation of Akt. The mutant PIK3CA (N1068fs*4) induced phosphorylation of Akt, but the level was comparable to that of wild type, and less than that of H1047R (Supplementary Fig. 6). These findings suggested that *Pik3ca* (N1068fs*4), as compared to H1047R, has less capacity for activating Akt and little

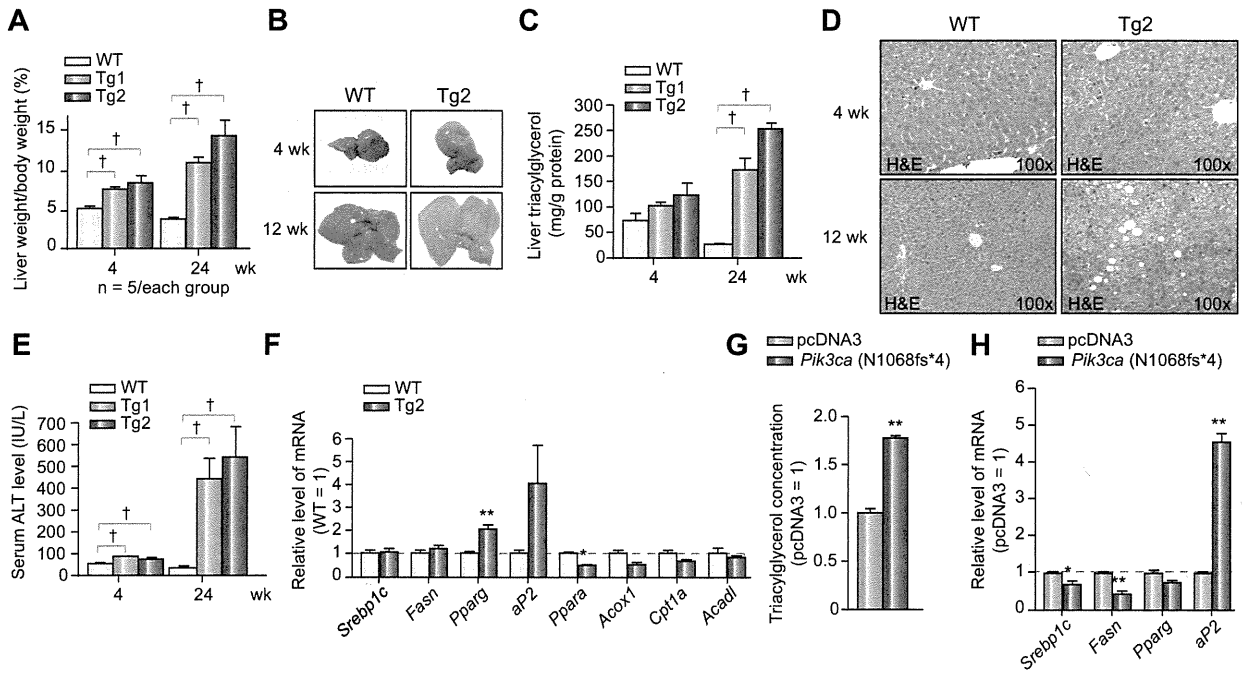

Fig. 2. Steatosis in the *Pik3ca* Tg liver. (A) Increased liver weight in *Pik3ca* Tg mice. (N = 5/group; †p <0.05, ANOVA; post hoc test with WT). (B) Representative liver images of WT and *Pik3ca* Tg mice. (C) High concentrations of intrahepatic triacylglycerol in the Tg mice (N >5/group; †p <0.05, ANOVA; post hoc test with WT). (D) H&E staining of livers from WT and *Pik3ca* Tg mice at 4 weeks (top) and 24 weeks (bottom) of age. (E) Higher serum ALT levels in the Tg mice (N = 5/group; †p <0.05, ANOVA; post hoc test with WT). (F) The expression of fat metabolism genes in the 4-week-old liver (N = 3–4/group; *p <0.05, **p <0.01, Student's t-test). (G) Cellular triacylglycerol levels and (H) the expression of lipogenesis-related genes in BNL-CL2 cells stably expressing *Pik3ca* (N1068fs*4) (N = 3/group; *p <0.05, **p <0.01, Student's t-test).

oncogenic activity in itself [13] and that there might be unknown factors promoting *in vivo* tumorigenesis in the *Pik3ca* Tg liver.

Downregulation of tumor suppressor genes in tumors derived from Pik3ca Tg livers

To further assess the related cellular signaling for tumorigenesis in the *Pik3ca* liver, we evaluated the activation of Akt, S6K, and Erk among the WT liver, non-tumor Tg liver, and tumor tissues from 52-week-old mice (Fig. 4A). Tumor tissues exhibited significantly enhanced activation of Akt compared to the Akt activation in non-tumor background or WT livers. We observed stronger phosphorylation of Akt in the non-tumor Tg liver than in WT livers, but the difference was not statistically significant as determined by ANOVA. Furthermore, the immunohistochemistry for phospho-Akt did not demonstrate clear differences between non-tumor livers and WT tissues. In contrast, the expression of *Myc-Pik3ca* was sustained in the non-tumor liver at 52 weeks (Supplementary Fig. 7). Those findings suggest the possibility that continuous activation of Akt induced by overexpressed *Pik3ca* is important for tumor formation in the Tg livers [31], whereas it remains unknown why Akt phosphorylation was attenuated in the non-tumor liver at 52 weeks despite the sustained expression of *Pik3ca* (Fig. 4A and Supplementary Fig. 7). In addition, the phosphorylation of S6K and Erk tended to be higher in Tg livers than in WT livers (Fig. 4A), but the difference became attenuated at 52 weeks compared to that at 4 weeks (Figs. 1B and 4A and Supplementary Fig. 8). These data do not exclude the possible role of these molecules in tumorigenesis in Tg livers but at least may emphasize the importance of Akt activation. Next, we examined the expression levels of genes involved in murine hepatotumorigenesis [32–34]. We observed decreased expression of four tumor suppressor genes, *Pten*, AT-rich interactive domain 5B (*Arid5b*), exportin 4 (*Xpo4*), and deleted in liver cancer 1 (*Dlc1*), in the tumor compared to the non-tumor background of *Pik3ca* Tg livers (Fig. 4B and Supplementary Fig. 9). PTEN protein levels were downregulated (Fig. 4C). To address whether the downregulation of *Pten* contributes to the tumorigenic activity in liver cells, we established *Pten*-depleted BNL-CL2 cells (Fig. 4D). *Pten*-depleted BNL-CL2 cells generated significantly more colonies in soft agar (Fig. 4E), indicative of enhanced tumorigenicity. These findings emphasize the possibility that the decreased expression of tumor suppressor genes has a certain role in tumorigenesis in the *Pik3ca* Tg liver. Importantly, the *in vitro* overexpression of mutant *Pik3ca* (N1068fs*4) only suppressed *Arid5b* expression but did not decrease the expression of *Pten*, *Xpo4*, or *Dlc1* in BNL-CL2 cells, indicating that certain additional mechanisms repressed their expression (Supplementary Fig. 10). Although several reports suggested a relationship between oxidative stress and hepatocarcinogenesis [35], the levels of hydrogen peroxide and lipid peroxidation were comparable between Tg and WT livers (Supplementary Fig. 11).

Tumors contain higher concentrations of OAs and palmitic acids (PAs) compared to the background tissues in the Pik3ca Tg liver

Recent intensive research has shed light into the significance of fatty acid (FA) as a potent biological stimulator of intracellular

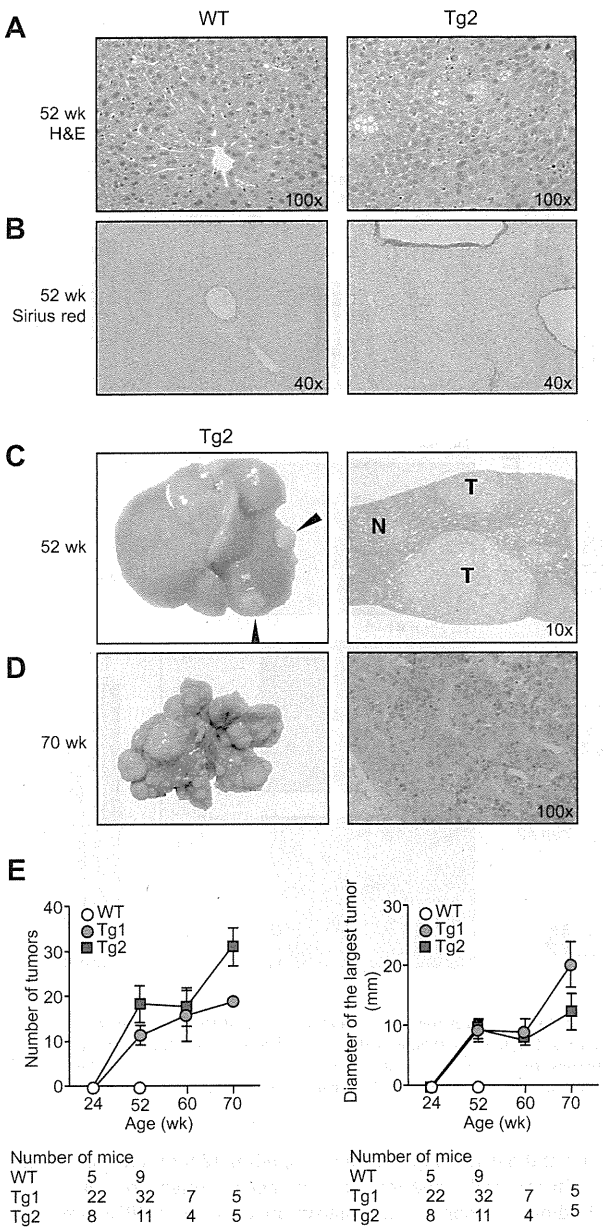

Fig. 3. Liver tumors in the *Pik3ca* Tg mice. (A) H&E and (B) Sirius red staining of livers at 52 weeks. (C) Macroscopic view (left) of the representative liver adenomas (arrowheads) at 52 weeks of age. H&E staining of an adenoma (T) and adjacent parenchyma (N) (right). (D) Tumors in *Pik3ca* Tg mice at 70 weeks (left). H&E staining of HCC (right). (E) The number (left) and size (right) of hepatic tumors. The number of mice examined is shown below the graphs.

signaling [36]. Interestingly, unsaturated FAs inhibit *Pten* expression via microRNA-21 in hepatoma [7,37,38], and the overexpression of a FA receptor (FFAR2) transformed the 3T3 fibroblasts [39], suggesting the possible relationship between FA and tumorigenesis. In the *Pik3ca* Tg liver, the tumor tissues contained higher concentrations of FAs than the non-tumor background tissues (Fig. 5A). The difference in total FA levels was largely due to the increase in levels of OA (C18:1n9) and PA (C16:0) in the tumors (Fig. 5B and C, Supplementary Fig. 12 and Table 2).

OA has the potential to repress the expression of tumor suppressors and enhance colony formation in vitro

To examine the possibility that either OA or PA downregulates the expression of tumor suppressors including *Pten*, we treated BNL-CL2 cells with OA or PA. OA, but not PA, repressed the expression of *Pten*, *Arid5b*, *Xpo4*, and *Dlc1* (Fig. 6A). Moreover, BNL-CL2 cells exposed to OA formed significantly more colonies in soft agar (Fig. 6B). These findings indicate that OA potentially enhances the in *vivo* tumorigenesis in the *Pik3ca* Tg liver. As an example, it is likely that decreased PTEN expression could enhance the Akt activation by the *Pik3ca* transgene in Tg-derived tumors (Fig. 1B).

Discussion

Hepatocyte-specific overexpression of *Pik3ca* (N1068fs*4) leads to steatosis and hepatic tumor formation. This mutation was originally isolated in human HCC and gastric cancers [12], but its functional analysis has never been reported. The *in vitro* overexpression of this mutant clearly induced Akt activation, but the level of activation was comparable with that of *Pik3ca* wild type and lower than that of the oncogenic H1047R mutant, suggesting that the *Pik3ca* Tg mice provide a model for studying effects of PIK3CA overexpression rather than a gain-of-function of PIK3CA. Furthermore, the N1068fs*4 mutation was not sufficient for cellular transformation *in vitro*, different from *Pik3ca* H1047R [40]. Considering results from a previous report suggesting the pivotal role of Akt activation in cell transformation by *PIK3CA* mutation [13], the activation level of Akt induced by *Pik3ca* (N1068fs*4) expression should not be sufficient for the cell-transforming process. These data indicated that the development of hepatic tumors in Tg mice might not be always a direct effect of *Pik3ca* (N1068fs*4) but instead promoted by other *in vivo* protumorigenic factors.

We focused on FA as an additional protumorigenic factor contributing to *in vivo* hepato-tumorigenesis in Tg mice, based on recent research on their oncogenic capacity [39]. Previous studies reported that OA inhibits *PTEN* expression via the upregulation of microRNA-21 through an mTOR/NF-κB-dependent mechanism [37,38] and also that exposure to OA increases tumor growth in xenografts [7]. Here, we demonstrated the correlation between OA accumulation and downregulation of other tumor suppressors, whereas the entire molecular mechanism remains to be elucidated. At least, there is a possibility that, in the Tg-derived tumors, OA accumulation enhanced the Akt activation by the *Pik3ca* transgene, which phosphorylates Akt less strongly than other oncogenic mutants *in vitro* (Fig. 1B, Supplementary Figs. 6 and 13).

Lipogenesis is mainly mediated by two major transcription factors, PPARγ and SREBP1C [24,25]. Hepatocyte-specific *Pten* KO mice exhibited increased expression of both PPARγ and SREBP1c in the liver, whereas only PPARγ was highly expressed in the *Pik3ca* Tg liver [16]. Our *in vitro* data suggested that the PI3K signaling is upstream of the activation of PPARγ in hepatocytes. A recent study shows that levels of *PPARγ* as well as *SREBP1c* mRNA are higher in the livers of patients with steatosis

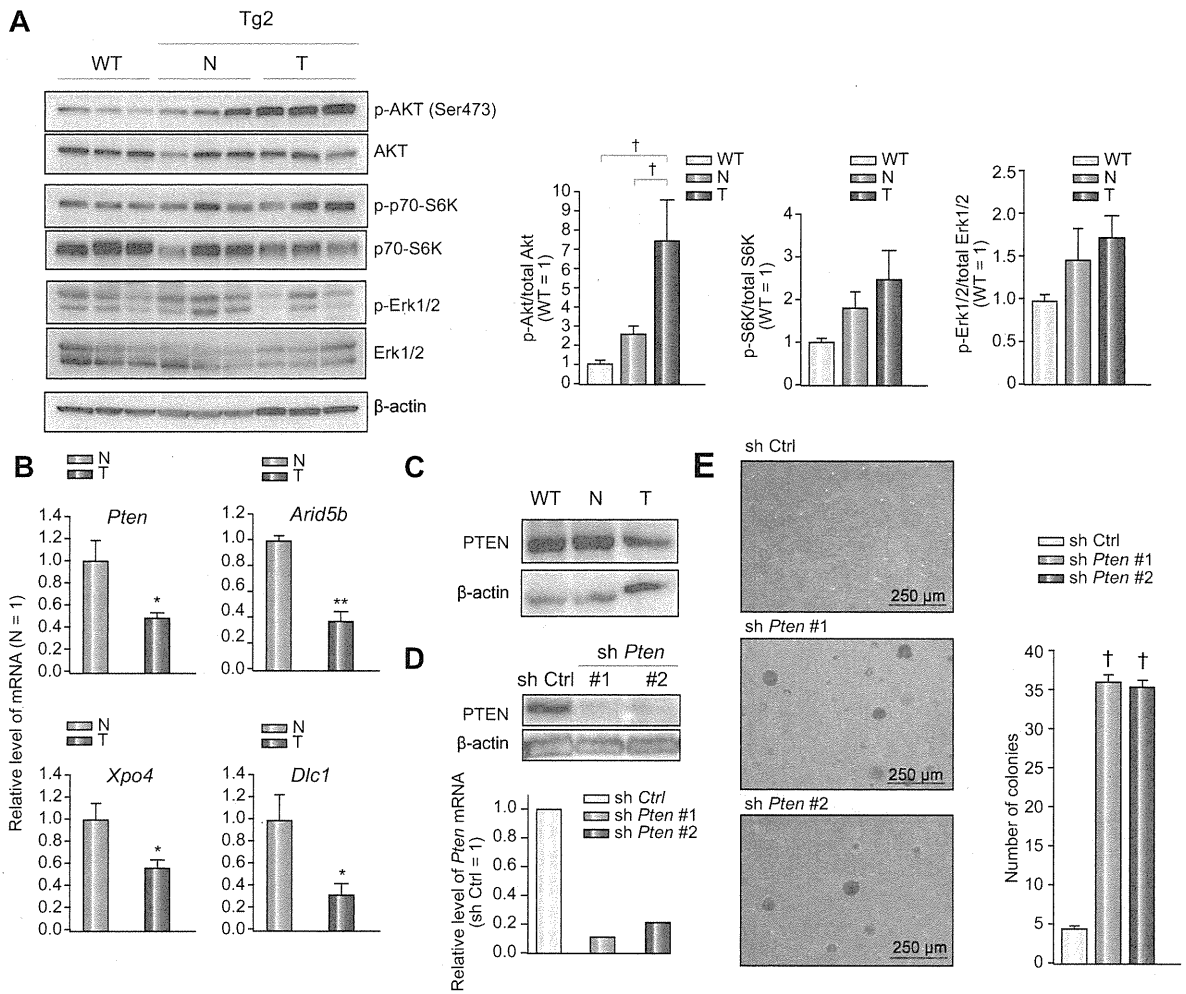

Fig. 4. *Pten* downregulation in the *Pik3ca* Tg liver. (A) Immunoblots and quantification of liver homogenates at 52 weeks ($^{\dagger}p$ <0.05, ANOVA; post hoc test with WT). (B) The decreased expression of *Pten*, *Arid5b*, *Xpo4*, and *Dlc1* mRNA in the *Pik3ca* Tg liver tumors (T) relative to their expression in background liver tissues (N) (N = 5/group; $^{*}p$ <0.05, $^{**}p$ <0.01, Student's *t*-test). (C) Representative images of immunoblots of liver tissues from the littermates at 52 weeks. (D) Knockdown of *Pten* in BNL-CL2 cells confirmed at the protein (top) and mRNA (bottom) levels. (E) Both lines of *Pten*-depleted BNL-CL2 cells (sh*Pten* #1 and #2) formed more colonies in soft agar (N = 3/group; † p <0.05, ANOVA; post hoc test with control cells (shCtrl)).

or steatohepatitis, suggesting that the activity of PPARγ is implicated in the abnormal lipid accumulation in human livers [41] (Supplementary Fig. 13).

Unlike the hepatocyte-specific *Pten* KO mice [16], cellular infiltration and fibrosis were not observed in the *Pik3ca* Tg liver. One explanation is the possibility that *Pten* deficiency induces certain pathological mechanisms independently of PI3K-Akt activation, as previously reported for mammary tumorigenesis [18–20,42–45]. Indeed, although genetic changes in PTEN result in potent Akt phosphorylation, *in vivo* studies have suggested that they show distinct phenotypes [42]. The conditional knockout of PTEN enhanced tumorigenesis in the mammary gland [43]; however, transgenic mice expressing constitutively active Akt in the mammary gland did not show tumor formation [44]. PTEN directly associates with p53, thereby increasing its stability, protein level, and transcriptional activity [18,19]. PTEN induces apoptosis and cell cycle arrest through PI3K/Akt-independent pathways [20]. PTEN also has important roles in integrin signaling and has the ability to dephosphorylate focal adhesion kinase, reducing cell adhesion and enhancing migration [46]. These findings support an alternative mechanism of PTEN-mediated tumorigenesis independent on PI3K/Akt pathway. As a second reason for the difference from *Pten* KO mice, it is possible that PI3K catalytic beta has a distinct role with PIK3CA in the phenotype of *Pten* deficiency [47].

The discrepancy between the scarce inflammatory levels in the *Pik3ca* Tg liver and the strong increase in serum ALT levels indicative of severe liver injury is to be solved in the near future. We found that inflammatory cytokine IL-1α and Fas ligand were more highly expressed in the *Pik3ca* Tg liver than in the WT liver (Supplementary Fig. 4). Taking into account reports demonstrating that these factors can lead to liver damage [28,29], it can be suggested that their abnormal upregulation in Tg livers is in part responsible for liver damage, whereas the entire molecular process inducing them remains unknown (Supplementary Fig. 13).

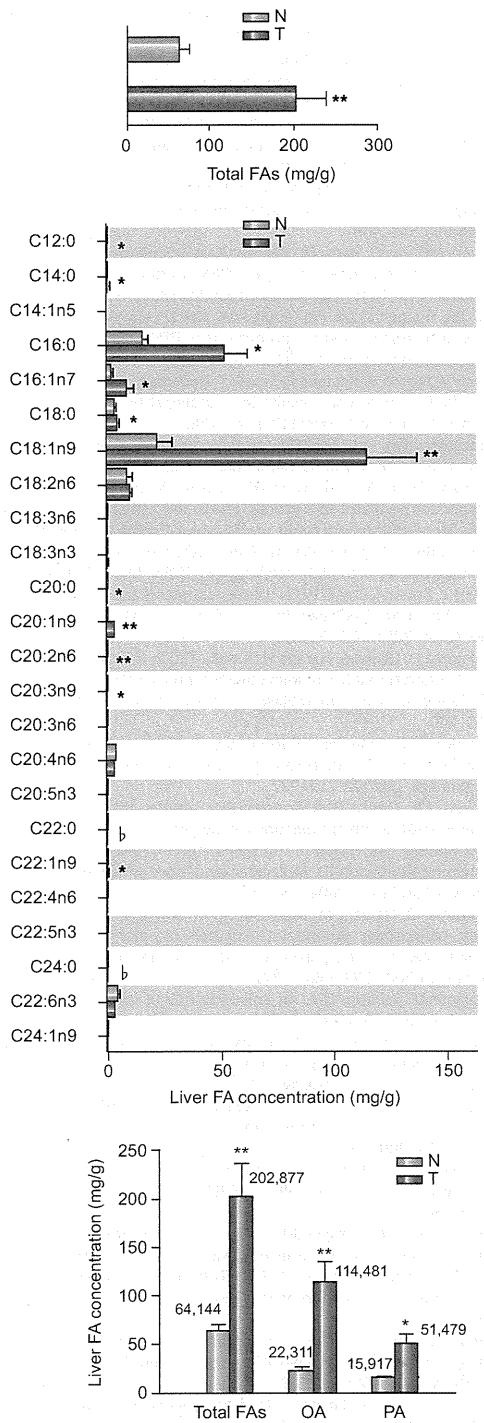

Fig. 5. The total FA composition in the *Pik3ca* Tg liver tissues and tumors. (A) The levels of FAs in the tumor (T) and non-tumor background tissue (N) in *Pik3ca* Tg mice at 52 weeks (N = 4/group; $^{**}p$ <0.01, Student's *t*-test). (B) FA composition in background (N) and tumor tissues (T) (N = 4/group; statistically increased FA levels in the tumors are shown with asterisks ($^{*}p$ <0.05, $^{**}p$ <0.01) and significantly decreased levels are shown with flat (μ, p <0.05), Student's *t*-test). (C) The concentration of total FAs, OA, and PA in background (N) and tumor tissues (T) (N = 4/group; $^{*}p$ <0.05, $^{**}p$ <0.01, Student's *t*-test).

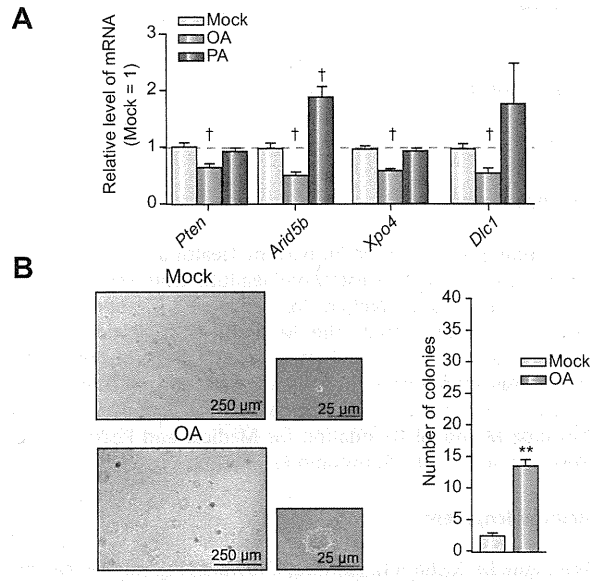

Fig. 6. OA enhances the colony-forming activity of immortalized hepatocytes. (A) OA but not PA decreased *Pten*, *Arid5b*, *Xpo4*, and *Dlc1* mRNA *in vitro* (N = 3/group; $^{\dagger}p$ <0.05, ANOVA; post hoc test with Mock group). (B) Colony formation assay of BNL-CL2 cells with or without 50 μmol/L OA in 10% or 0.5% FBS media (N = 3/group; $^{**}p$ <0.01, Student's *t*-test).

Mechanisms involved in the pathogenesis of non-alcoholic steatohepatitis (NASH) remain unclear, but the "two-hit theory" is widely accepted [48]. That is, in the first hit, insulin-resistance is followed by lipid accumulation in the liver, and the second hit, possibly involving inflammatory cytokines or oxidative stress, results in hepatic injury and fibrosis. It has been reported that ROS has certain roles in *in vivo* carcinogenesis [35], and the concentration of ROS is upregulated in the liver suffering NASH or NASH-derived HCC [49]. Regardless of the obvious fatty liver, our model mice have not shown impaired glucose tolerance. The concentration of ROS in the *Pik3ca* Tg mice was comparable with that of WT mice (Supplementary Fig. 11), which can be partly explained by the lower expression of fat-oxidative genes (Fig. 2F) and lack of inflammatory cell infiltration. These findings indicate that *Pik3ca* Tg mice do not always mimic the entire pathological mechanisms causing NASH, while they might be useful as a prototype to determine which pathological processes are required for the progression from the fatty liver to NASH. In addition, given the low rate of HCC development in these mice, they can be potentially useful for discovering tumor-promoting factors in hepatic steatosis. For example, although it was unlikely that ROS is involved in the initiation of hepatic tmor in the *Pik3ca* Tg liver, we can examine the pathological significance of ROS in tumor progression as well as hepatitis induction by applying the *Pik3ca* Tg liver to the condition producing high levels of ROS.

Recent clinical findings have advocated the relationship between volume of visceral fat and tumor progression [1–4]. While there is no direct molecular evidence to address the notion that abnormal body fat accumulation accelerates tumor growth, our data might provide new insights into the mechanisms of the "lipotoxicity-related" tumorigenesis. Future researches are needed to unravel how OA affects gene expression.

Conflict of interest

The authors who have taken part in this study declared that they do not have anything to disclose regarding funding or conflict of interest with respect to this manuscript.

Financial support

This study was supported, in part, by Health and Labor Sciences Research Grants for Research on Hepatitis from the Ministry of Health, Labor, and Welfare of Japan, by Grants-in-Aid for Scientific Research from the Ministry of Education, Culture, Sports, Science, and Technology of Japan, by The Mishima-Kaiun foundation, by the Ichiro Kanehara Foundation, by Sankyo Foundation of Life Science, by Takeda Science Foundation, by The Mochida Memorial Foundation for Medical and Pharmaceutical Research and by The Sumitomo Foundation.

Acknowledgments

We thank Dr. Richard D. Palmiter (Howard Hughes Medical Institute and Department of Biochemistry, University of Washington, Seattle, USA) and Francis V. Chisari (Department of Molecular and Experimental Medicine, Scripps Research Institute, La Jolla, USA) for providing the plasmid. We also thank Dr. Junji Shibahara (Department of Pathology, Graduate School of Medicine, The University of Tokyo) and Kojiro Ueki (Department of Metabolic Diseases, Graduate School of Medicine, The University of Tokyo) for helpful discussions, and Mitsuko Tsubouchi for technical assistance.

Supplementary data

Supplementary data associated with this article can be found, in the online version, at doi:10.1016/j.jhep.2011.03.025.

References

[1] Garfinkel L. Overweight and cancer. Ann Intern Med 1985;103:1034–1036.
[2] Deslypere JP. Obesity and cancer. Metabolism 1995;44:24–27.
[3] Schapira DV, Clark RA, Wolff PA, Jarrett AR, Kumar NB, Aziz NM. Visceral obesity and breast cancer risk. Cancer 1994;74:632–639.
[4] Yamaji Y, Okamoto M, Yoshida H, Kawabe T, Wada R, Mitsushima T, et al. The effect of body weight reduction on the incidence of colorectal adenoma. Am J Gastroenterol 2008;103:2061–2067.
[5] Hill-Baskin AE, Markiewski MM, Buchner DA, Shao H, DeSantis D, Hsiao G, et al. Diet-induced hepatocellular carcinoma in genetically predisposed mice. Hum Mol Genet 2009;18:2975–2988.
[6] Park EJ, Lee JH, Yu GY, He G, Ali SR, Holzer RG, et al. Dietary and genetic obesity promote liver inflammation and tumorigenesis by enhancing IL-6 and TNF expression. Cell 2010;140:197–208.
[7] Vinciguerra M, Carrozzino F, Peyrou M, Carlone S, Montesano R, Benelli R, et al. Unsaturated fatty acids promote hepatoma proliferation and progression through downregulation of the tumor suppressor PTEN. J Hepatol 2009;50:1132–1141.
[8] Engelman JA, Luo J, Cantley LC. The evolution of phosphatidylinositol 3-kinases as regulators of growth and metabolism. Nat Rev Genet 2006;7:606–619.
[9] Bader AG, Kang S, Zhao L, Vogt PK. Oncogenic PI3K deregulates transcription and translation. Nat Rev Cancer 2005;5:921–929.
[10] Vivanco I, Sawyers CL. The phosphatidylinositol 3-kinase AKT pathway in human cancer. Nat Rev Cancer 2002;2:489–501.
[11] Samuels Y, Diaz Jr LA, Schmidt-Kittler O, Cummins JM, Delong L, Cheong I, et al. Mutant PIK3CA promotes cell growth and invasion of human cancer cells. Cancer cell 2005;7:561–573.
[12] Lee JW, Soung YH, Kim SY, Lee HW, Park WS, Nam SW, et al. PIK3CA gene is frequently mutated in breast carcinomas and hepatocellular carcinomas. Oncogene 2005;24:1477–1480.
[13] Ikenoue T, Kanai F, Hikiba Y, Obata T, Tanaka Y, Imamura J, et al. Functional analysis of PIK3CA gene mutations in human colorectal cancer. Cancer Res 2005;65:4562–4567.
[14] Myers MP, Pass I, Batty IH, Van der Kaay J, Stolarov JP, Hemmings BA, et al. The lipid phosphatase activity of PTEN is critical for its tumor suppressor function. Proc Natl Acad Sci USA 1998;95:13513–13518.
[15] Hu TH, Huang CC, Lin PR, Chang HW, Ger LP, Lin YW, et al. Expression and prognostic role of tumor suppressor gene PTEN/MMAC1/TEP1 in hepatocellular carcinoma. Cancer 2003;97:1929–1940.
[16] Horie Y, Suzuki A, Kataoka E, Sasaki T, Hamada K, Sasaki J, et al. Hepatocyte-specific Pten deficiency results in steatohepatitis and hepatocellular carcinomas. J Clin Invest 2004;113:1774–1783.
[17] Vinciguerra M, Foti M. PTEN at the crossroad of metabolic diseases and cancer in the liver. Ann Hepatol 2008;7:192–199.
[18] Freeman DJ, Li AG, Wei G, Li HH, Kertesz N, Lesche R, et al. PTEN tumor suppressor regulates p53 protein levels and activity through phosphatase-dependent and -independent mechanisms. Cancer Cell 2003;3:117–130.
[19] Li AG, Piluso LG, Cai X, Wei G, Sellers WR, Liu X. Mechanistic insights into maintenance of high p53 acetylation by PTEN. Mol Cell 2006;23:575–587.
[20] Weng L, Brown J, Eng C. PTEN induces apoptosis and cell cycle arrest through phosphoinositol-3-kinase/Akt-dependent and -independent pathways. Hum Mol Genet 2001;10:237–242.
[21] Nakajima O, Okano S, Harada H, Kusaka T, Gao X, Hosoya T, et al. Transgenic rescue of erythroid 5-aminolevulinate synthase-deficient mice results in the formation of ring sideroblasts and siderocytes. Genes Cells 2006;11:685–700.
[22] Pasquinelli C, Shoenberger JM, Chung J, Chang KM, Guidotti LG, Selby M, et al. Hepatitis C virus core and E2 protein expression in transgenic mice. Hepatology 1997;25:719–727.
[23] Pinkert CA, Ornitz DM, Brinster RL, Palmiter RD. An albumin enhancer located 10 kb upstream functions along with its promoter to direct efficient, liver-specific expression in transgenic mice. Genes Dev 1987;1:268–276.
[24] Browning JD, Horton JD. Molecular mediators of hepatic steatosis and liver injury. J Clin Invest 2004;114:147–152.
[25] Gavrilova O, Haluzik M, Matsusue K, Cutson JJ, Johnson L, Dietz KR, et al. Liver peroxisome proliferator-activated receptor gamma contributes to hepatic steatosis, triglyceride clearance, and regulation of body fat mass. J Biol Chem 2003;278:34268–34276.
[26] Laplante M, Sabatini DM. An emerging role of mTOR in lipid biosynthesis. Curr Biol 2009;19:R1046–R1052.
[27] Patek PQ, Collins JL, Cohn M. Transformed cell lines susceptible or resistant to in vivo surveillance against tumorigenesis. Nature 1978;276:510–511.
[28] Sakurai T, He G, Matsuzawa A, Yu G-Y, Maeda S, Hardiman G, et al. Hepatocyte necrosis induced by oxidative stress and IL-1α release mediate carcinogen-induced compensatory proliferation and liver tumorigenesis. Cancer Cell 2008;14:156–165.
[29] Ogasawara J, Watanabe-Fukunaga R, Adachi M, Matsuzawa A, Kasugai T, Kitamura Y, et al. Lethal effect of the anti-Fas antibody in mice. Nature 1993;364:806–809.
[30] Gymnopoulos M, Elsliger MA, Vogt PK. Rare cancer-specific mutations in PIK3CA show gain of function. Proc Natl Acad Sci USA 2007;104:5569–5574.
[31] Aoki M, Batista O, Bellacosa A, Tsichlis P, Vogt PK. The Akt kinase: molecular determinants of oncogenicity. Proc Natl Acad Sci USA 1998;95:14950–14955.
[32] Zender L, Xue W, Zuber J, Semighini CP, Krasnitz A, Ma B, et al. An oncogenomics-based in vivo RNAi screen identifies tumor suppressors in liver cancer. Cell 2008;135:852–864.
[33] Xue W, Krasnitz A, Lucito R, Sordella R, Vanaelst L, Cordon-Cardo C, et al. DLC1 is a chromosome 8p tumor suppressor whose loss promotes hepatocellular carcinoma. Genes Dev 2008;22:1439–1444.
[34] Zeng Q, Hong W. The emerging role of the hippo pathway in cell contact inhibition, organ size control, and cancer development in mammals. Cancer Cell 2008;13:188–192.
[35] Ishii H, Horie Y, Ohshima S, Anezaki Y, Kinoshita N, Dohmen T, et al. Eicosapentaenoic acid ameliorates steatohepatitis and hepatocellular carcinoma in hepatocyte-specific Pten-deficient mice. J Hepatol 2009;50:562–571.

[36] Suganami T, Tanimoto-Koyama K, Nishida J, Itoh M, Yuan X, Mizuarai S, et al. Role of the Toll-like receptor 4/NF-kappaB pathway in saturated fatty acid-induced inflammatory changes in the interaction between adipocytes and macrophages. Arterioscler Thromb Vasc Biol 2007;27:84–91.
[37] Vinciguerra M, Veyrat-Durebex C, Moukil MA, Rubbia-Brandt L, Rohner-Jeanrenaud F, Foti M. PTEN down-regulation by unsaturated fatty acids triggers hepatic steatosis via an NF-kappaBp65/mTOR-dependent mechanism. Gastroenterology 2008;134:268–280.
[38] Vinciguerra M, Sgroi A, Veyrat-Durebex C, Rubbia-Brandt L, Buhler LH, Foti M. Unsaturated fatty acids inhibit the expression of tumor suppressor phosphatase and tensin homolog (PTEN) via microRNA-21 up-regulation in hepatocytes. Hepatology 2009;49:1176–1184.
[39] Hatanaka H, Tsukui M, Takada S, Kurashina K, Choi YL, Soda M, et al. Identification of transforming activity of free fatty acid receptor 2 by retroviral expression screening. Cancer Sci 2010;101:54–59.
[40] Kang S, Bader AG, Vogt PK. Phosphatidylinositol 3-kinase mutations identified in human cancer are oncogenic. Proc Natl Acad Sci USA 2005; 102:802–807.
[41] Pettinelli P, Videla LA. Up-regulation of PPAR-γ mRNA expression in the liver of obese patients: an additional reinforcing lipogenic mechanism to SREBP-1c induction. J Clin Endocrinol Metab 2011;96:1424–1430.
[42] Blanco-Aparicio C, Renner O, Leal JF, Carnero A. PTEN, more than the AKT pathway. Carcinogenesis 2007;28:1379–1386.
[43] Li G, Robinson GW, Lesche R, Martinez-Diaz H, Jiang Z, Rozengurt N, et al. Conditional loss of PTEN leads to precocious development and neoplasia in the mammary gland. Development 2002;129:4159–4170.
[44] Ackler S, Ahmad S, Tobias C, Johnson MD, Glazer RI. Delayed mammary gland involution in MMTV-AKT1 transgenic mice. Oncogene 2002;21: 198–206.
[45] Hutchinson J, Jin J, Cardiff RD, Woodgett JR, Muller WJ. Activation of Akt (protein kinase B) in mammary epithelium provides a critical cell survival signal required for tumor progression. Mol Cell Biol 2001;21:2203–2212.
[46] Tamura M, Gu J, Matsumoto K, Aota S, Parsons R, Yamada KM. Inhibition of cell migration, spreading, and focal adhesions by tumor suppressor PTEN. Science 1998;280:1614–1617.
[47] Jia S, Liu Z, Zhang S, Liu P, Zhang L, Lee SH, et al. Essential roles of PI(3)K-p110beta in cell growth, metabolism and tumorigenesis. Nature 2008;454: 776–779.
[48] Day CP, James OF. Steatohepatitis: a tale of two "hits"? Gastroenterology 1998;114:842–845.
[49] Malaguarnera L, Madeddu R, Palio E, Arena N, Malaguarnera M. Heme oxygenase-1 levels and oxidative stress-related parameters in non-alcoholic fatty liver disease patients. J Hepatol 2005;42:585–591.

Journal of Gastroenterology and Hepatology

JGHF

doi:10.1111/j.1440-1746.2010.06559.x

HEPATOLOGY

Utility of contrast-enhanced ultrasonography with Sonazoid in radiofrequency ablation for hepatocellular carcinoma

Ryota Masuzaki,* Shuichiro Shiina,* Ryosuke Tateishi,* Haruhiko Yoshida,* Eriko Goto,* Yosuke Sugioka,† Yuji Kondo,* Tadashi Goto,* Hitoshi Ikeda,† Masao Omata‡ and Kazuhiko Koike*

*Graduate School of Medicine, Department of Gastroenterology, The University of Tokyo, †Department of Clinical Laboratory, The University of Tokyo Hospital, Tokyo ‡Yamanashi Prefectural Hospital Organization, Kofu, Japan

Key words
contrast-enhanced ultrasonography, hepatocellular carcinoma, radiofrequency ablation.

Accepted for publication 23 October 2010.

Correspondence
Haruhiko Yoshida, Department of Gastroenterology, University of Tokyo, 7-3-1 Hongo, Bunkyo-ku, Tokyo 113-8655, Japan.
Email: yoshida-2im@h.u-tokyo.ac.jp

The authors do not have any financial or other relationships to disclose.

Abbreviations
CEUS, contrast-enhanced ultrasonography; CT, computed tomography; HCC, hepatocellular carcinoma; RFA, radiofrequency ablation; US, ultrasonography.

Abstract

Background and Aims: Kupffer imaging in contrast-enhanced ultrasonography (CEUS) with Sonazoid, which lasts for 60 min or longer, may be useful in ultrasound-guided percutaneous tumor ablation. The utility of Sonazoid in radiofrequency ablation (RFA) of hepatocellular carcinoma (HCC) was investigated in this study.
Methods: We analyzed a total of 716 HCC nodules that were detected on dynamic computed tomography in 316 patients. Detectability of these nodules was compared between CEUS and conventional ultrasonography. The effectiveness in the treatment was assessed by comparing the mean numbers of treatment sessions of RFA in patients treated with CEUS and that in historical controls matched for tumor and background conditions.
Results: Detectability of tumor nodule was 83.5% in conventional ultrasonography and 93.2% in CEUS ($P = 0.04$). Sixty-nine nodules in 52 patients were additionally detected with CEUS. The number of additionally detected tumor nodules was positively correlated with serum albumin level ($P = 0.016$). The number of RFA sessions was 1.33 ± 0.45 with CEUS as compared to 1.49 ± 0.76 in the historical controls ($P = 0.0019$).
Conclusions: CEUS with Sonazoid is useful for HCC detection in patients with a well-conserved liver function reservoir. The decrease in RFA session numbers indicated the utility of Sonazoid in RFA treatment of HCC.

Introduction

Hepatocellular carcinoma (HCC) is the sixth most common cancer worldwide and the third most frequent cause of cancer death.[1] Because potentially curative treatments can be indicated only at less advanced stages, detection of HCC at an early stage is still a prerequisite for improved prognosis.[2] Recently, radiofrequency ablation (RFA) has been introduced and accepted as an effective nonsurgical treatment for HCC,[3–5] showing 5-year survival rates exceeding 50%.[6] RFA is potentially curative, minimally invasive, and easily repeatable in case of recurrence.

Real-time visualization of the target lesion is sine qua non for percutaneous ultrasound-guided ablation therapies, including RFA. However, visualization is sometimes difficult because of shape changes and coarse parenchymal echogenicity in cirrhotic liver.[7] Virtual sonographic images reconstructed from multidetector-row computed tomography (CT) images are useful for HCC nodules that are not depicted by conventional ultrasonography (US).[8] However, virtual sonographic images do not always precisely correspond to the real-time US images because of locational and morphological changes in the liver caused by respiration, postural movement, or bowel peristalsis. Although CT-guided RFA is thought to be useful for such nodules, real-time visualization is inferior to US guidance and accompanied by radiation exposure to operators and patients.[9] Several contrast materials have been developed to improve US resolution and have indeed been shown to be useful in differential diagnosis of hepatic tumorous lesions.[10,11] However, their role in percutaneous ablation is limited because of the short-lasting enhancement effect.

A second-generation sonographic contrast agent, Sonazoid (Daiichi-Sankyo, Tokyo, Japan), a lipid stabilized suspension of perfluorobutane gas microbubbles, has been used clinically in Japan since January 2007 in patients with liver tumors, with phase inversion harmonic gray scale sonography.[12,13] The perfluorobutane microbubbles are taken up by Kupffer cells in the liver sinusoid, allowing parenchyma-specific imaging of the liver. This imaging, called Kupffer imaging, is typically presented 10 min after injection of Sonazoid, when lesions that contain few Kupffer cells are clearly delineated as contrast defect surrounded by enhanced normal hepatic parenchyma. Kupffer imaging is particularly useful in detecting HCC nodules, which typically lack Kupffer cells. Moreover, contrast-enhanced ultrasonography

© 2011 Journal of Gastroenterology and Hepatology Foundation and Blackwell Publishing Asia Pty Ltd

(CEUS) with Sonazoid can be expected to be useful also in ultrasound-guided percutaneous ablation, including RFA, because Kupffer imaging lasts usually for more than 60 min. However, there are few reports about the utility of Sonazoid as a contrast agent during RFA of HCC.[14,15]

The aim of the present study was to evaluate the utility of the contrast agent Sonazoid in ultrasound-guided percutaneous RFA of HCC in terms of HCC nodule detection. Overall facilitation of the ablation procedure was also evaluated by comparing the numbers of RFA sessions per treatment between RFA using CEUS with Sonazoid and matched historical controls that had used conventional US.

Methods

Patients

We analyzed a total of 716 HCC nodules in 316 consecutive patients who were admitted for RFA between July 2007 and December 2007. All patients were treated on an inpatient basis. In every case, CEUS was carried out the day before RFA. Detection of HCC nodules was compared between CEUS and conventional US, using dynamic CT as the reference standard. In 291 patients, CEUS was carried out also during RFA. We assessed whether CEUS facilitated RFA by comparing the numbers of RFA sessions per treatment in CEUS-assisted RFA and in historical controls matched for tumor and background conditions, performed with conventional US between January 2004 and July 2007. The study protocol conformed to the ethical guidelines of the Helsinki Declaration 2004 and was approved by the research ethics committee of the authors' institution.

Diagnosis of HCC

HCC was diagnosed by dynamic CT, considering hyperattenuation in the arterial phase with washout in the late phase as a definite finding.[16] Multidetector-row CT (MDCT) was performed within a month before RFA, where plain and dynamic contrast-enhanced CT images were obtained with rapid intravenous injection of a contrast material. MDCT systems used for our study were Aquillion 64 (Toshiba, Tokyo, Japan) or LightSpeed VCT (GE Healthcare, Milwaukee, WI, USA). A bolus of iodinated contrast material was injected using a mechanical power injector in 30 s, at a concentration of 300–370 mg I/mL for the amount of bodyweight (kg) $\times$ 2 mL (maximum, 100 mL). The three contrast-enhanced phases (early arterial phase, late arterial phase, and equilibrium phase) were obtained at 25, 40, and 120 s after the start of injection. Reconstruction images were obtained with a section thickness of 2.5 mm with a reconstruction interval of 1.5 mm. Most HCC nodules were also confirmed histopathologically with ultrasound-guided biopsy afterwards. The pathological grade was evaluated based on Edmondson–Steiner criteria.[17]

Ultrasound examinations

All US examinations were carried out using the SSA-770A apparatus (APLIO; Toshiba, Tokyo, Japan), on patients after at least 5 h of fasting. First, we examined the liver for HCC lesions with conventional tissue harmonic imaging. We performed both intercostal and subcostal scans of the right lobe, and both sagittal and transverse scans of the left lobe. Efforts were exerted to maximize visualization of lesions, including positional changes and breath holding. Then, CEUS was performed by the same operator with phase inversion mode imaging. A 0.5-mL dose of Sonazoid was injected into an antebrachial vein at 0.2 mL/s via a 21-gauge cannula, followed by 20-mL of normal saline. The whole liver was scanned with CEUS, using similar techniques as used in the conventional US, 10 min after Sonazoid injection. When visualization was not sufficient at that time, a CEUS scan was repeated after a 5–10-min interval. Findings in conventional US and CEUS were separately recorded by the operator. Detection ability of US and CEUS was calculated using dynamic CT as a reference standard. We analyzed the correlation between the number of additionally detected nodules by CEUS and liver function reservoir, as represented by serum albumin concentration.

RFA sessions

Inclusion criteria for percutaneous ablation were as follows: total bilirubin concentration lower than 3 mg/dL; platelet count not less than $50 \times 10^3/mm^3$; and prothrombin activity not lower than 50%. Patients with portal vein tumor thrombosis, refractory ascites, or extrahepatic metastasis were excluded. The procedure has been meticulously described elsewhere.[18] In brief, grounding was achieved by attaching two pads to the patient's thighs. A 17-gauge, cooled-tip electrode with a 2- or 3-cm exposed tip was attached to a radiofrequency generator (Covidien, Mansfield, MA, USA). After local anesthesia, the electrode was inserted under ultrasound guidance. During ablation, the temperature was measured with a thermocouple in the electrode and tissue impedance was also monitored by a circuitry incorporated into the generator. A peristaltic pump infused 0°C saline into the electrode lumen to maintain the tip temperature below 20°C. Radiofrequency energy was delivered for 6–12 min on each application. A 12-min ablation using a 3-cm electrode would produce a quasi-spherical necrotic volume 3 cm in diameter. For larger lesions, the electrode was repeatedly inserted into different sites, so that the entire lesion could be enveloped by assumed necrotic volumes.

CEUS-assisted RFA was done basically with Kupffer imaging at least 10 min after Sonazoid injection. Electrodes were inserted after perfluorobutane microbubbles disappeared from vessels so that the vessels were well visualized. Before the introduction of CEUS, when a nodule was not well visualized by conventional US, the needle was inserted by real-time ultrasound reference to the portal vein or hepatic vein near the target nodule.

The efficacy of RFA was assessed with contrast-enhanced CT performed on the next day. Complete ablation was defined as hypoattenuation of each lesion with a sufficient safety margin in the surrounding liver parenchyma. When ablation was found to be insufficient, an additional session of RFA was carried out, until complete ablation was confirmed on contrast-enhanced CT. The number of RFA sessions was defined as the total number of intervention episodes required to achieve complete ablation.

Follow up

Each patient was followed up with contrast-enhanced CT every 4 months. Tumor recurrence was diagnosed according to the

© 2011 Journal of Gastroenterology and Hepatology Foundation and Blackwell Publishing Asia Pty Ltd

same criteria applied to initial HCC diagnosis. Intrahepatic recurrence was classified as either recurrence at a site distant from the primary site or that adjacent to the treated lesion (local tumor progression).

Historical controls

One historical control was selected for each patient who underwent CEUS-assisted RFA from patients who received RFA between January 2004 and July 2007, that is, prior to the introduction of CEUS ($n = 2261$). The maximum diameter of tumors (± 0.3 cm), the number of lesions (exact), viral markers (exact), and serum albumin concentration (± 0.3 g/dL) were used as the matching factors, with the maximum permissible differences shown in parentheses. The selection was carried out using the find-matches function of S-Plus 2000 (TIBCO Software, Palo Alto, CA, USA).

Statistical analysis

Variables were expressed as mean ± standard deviation unless otherwise specified. Continuous variables were compared using the unpaired Student's *t*-test, and categorical variables were compared using Fisher's exact probability test. The number of RFA sessions per patient was compared using the Mann–Whitney *U*-test. All tests were two-sided with a significance level of 5%. Statistical analyses were carried out with S-plus 2000.

Results

The baseline characteristics of patients who underwent CEUS are shown in Table 1. The patients consisted of 216 men and 100 women with a mean age of 70.1 ± 7.7 years. The mean maximum diameter of tumors was 1.6 ± 0.8 cm. All 316 patients underwent both conventional US and CEUS, in this order, the day before scheduled RFA. Of 716 HCC nodules diagnosed on dynamic CT, conventional US identified 598 (83.5%) nodules as definite lesions. Subsequent CEUS detected an additional 69 nodules, increasing the detectability to 93.2%, and the difference was statistically significant ($P = 0.04$). The number of additionally detected nodules per patient was one in 36 patients, two in eight, three in five, and more than three in three; thus at least one nodule was additionally detected with CEUS in a total of 52 patients (16.5%). Among these patients, artificial pleural effusion was used in 19 cases and artificial ascites was used in four patients, resulting in additional detection of 28 and four nodules, respectively. The number of additionally detected nodules by CEUS was positively correlated with serum albumin concentration ($P = 0.016$) (Fig. 1).

CEUS was also used during the RFA session in 291 patients. Artificial pleural effusion was performed in 71 (24.4%) cases and artificial ascites was used in 27 (9.1%) cases. Two demonstrative cases successfully treated with CEUS-assisted RFA are shown in Figures 2 and 3. We did not conduct randomization on the use of CEUS because its usefulness in tumor visualization was obvious at least in a proportion of the patients. Instead, we chose historical controls matched for tumor-related factors and liver function, and compared the number of RFA sessions per patient and total ablation time per session. In all patients including controls, RFA sessions were repeated until complete ablation of each nodule was confirmed on contrast-enhanced CT. The mean number of RFA sessions per patient was 1.33 ± 0.45 in patients with CEUS, as compared to 1.49 ± 0.76 in the historical controls ($P = 0.0019$ by Mann–Whitney *U*-test) (Table 2). Total ablation time per session was 17.2 ± 10.7 min with CEUS-assisted RFA and 15.7 ± 9.6 min in the historical controls ($P = 0.156$ by Mann–Whitney *U*-test). Treatment-related complications occurred in six patients (1.9%) who received CEUS-assisted RFA: peritoneal bleeding in three patients and hemothorax, bile duct bleeding, and dermal burn each in one patient. There was no treatment-related death. The incidence of complications did not differ in the historical controls (1.7%, $P = 0.867$ by Fisher's exact probability test). During the follow up, local tumor progression was detected in six patients (2.1%) who received CEUS-assisted RFA and in eight

Table 1 Baseline characteristics ($n = 316$)

Variables	
Age (years)†	70.1 ± 7.7
Male, *n* (%)	216 (68.3)
HBsAg positive, *n* (%)	45 (14.2)
HCVAb positive, *n* (%)	238 (75.3)
Diameter (cm)†	1.6 ± 0.8
Number of tumors	
1, *n* (%)	124 (39.3)
2–3, *n* (%)	143 (45.2)
≥ 4, *n* (%)	49 (15.5)
Total bilirubin (mg/dL)‡	0.9 (0.6–1.2)
Albumin (g/dL)‡	3.6 (3.2–3.9)
Platelet count (10^4/mm^3)‡	10.5 (7.3–13.8)
AFP (ng/mL)‡	16.9 (6.0–62.8)
L3 (%)‡	0.5 (0–3.1)
DCP (mAU/mL)‡	20 (13–50)

†Mean ± standard deviation.
‡Median (25th–75th percentiles).
AFP, alpha-fetoprotein; DCP, des-gamma-carboxy-prothrombin; HBsAg, hepatitis B surface antigen; HCVAb, hepatitis C virus antibody.

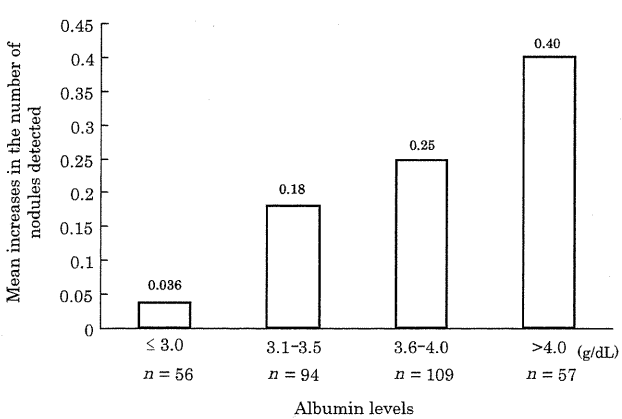

Figure 1 The mean increases in detected tumor number with contrast-enhanced ultrasonography were well correlated with serum albumin level ($P = 0.016$).

© 2011 Journal of Gastroenterology and Hepatology Foundation and Blackwell Publishing Asia Pty Ltd

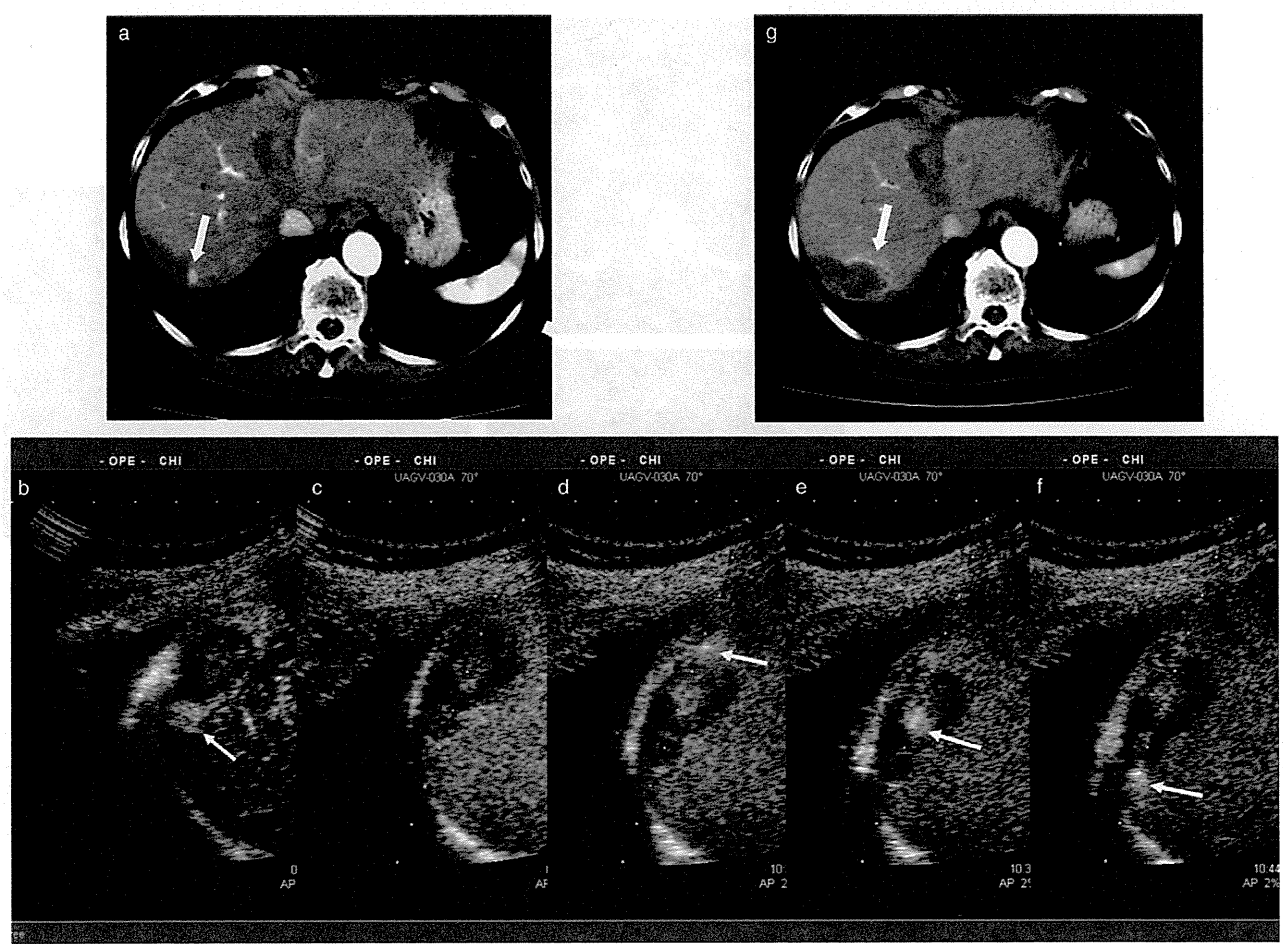

Figure 2 (a) An 80-year-old woman with hepatocellular carcinoma. Computed tomography (CT) revealed a nodule with hyperattenuation in the early arterial phase near a previously ablated lesion. (b) After injection of Sonazoid with artificial right pleural effusion, the nodule was clearly detected as a hyperechoic lesion (arrows). (c–f) Radiofrequency ablation of the nodule. (Arrows indicate the tip of radiofrequency needle). (g) Evaluation CT confirmed that the nodule was sufficiently ablated.

historical controls (2.7%, $P = 0.788$ by Fisher's exact probability test).

Discussion

In the present study, we have shown that the number of RFA sessions required per patient was significantly decreased when using the new US contrast agent, Sonazoid, as compared to historical controls. These were accomplished without increasing the incidence of local tumor progression or treatment-related complications. At the authors' institution, RFA is repeated until complete ablation of each HCC nodule is confirmed by dynamic CT. Without CEUS, when the tumor was not well delineated on conventional US, ablation used to be performed based on the information on CT and indecisive US images, which may have led to insufficient ablation revealed by evaluation CT, requiring an additional ablation session. Thus it can be assumed that the decreased number of RFA sessions with Sonazoid is mainly due to improvement in tumor detection and delineation. Unnecessary ablation of non-cancerous liver parenchyma may have deleterious effects on liver function and may reduce survival time. Thus the decrease in the number of RFA sessions is beneficial not only in cost reduction but possibly also for patients' survival.

The detectability of HCC nodules was increased from 83.5% to 93.2% with the use of CEUS, as determined with contrast CT as the reference standard. The benefit of using Sonazoid to detect "invisible" nodules by conventional US was more apparent in those with higher serum albumin concentration, suggesting that the resolution of Sonazoid CEUS may be compromised when liver function is substantially impaired. Uptake of perfluorobutane in non-cancerous liver depends on Kupffer cell function, which may be severely impaired in advanced liver diseases. A similar phenomenon was also reported in super paramagnetic iron oxide (SPIO)-enhanced magnetic resonance imaging.[19] Thus the contrast between HCC and non-cancerous parenchyma in Kupffer imaging can be diminished when liver function reservoir is poor. In the present study we obtained Kupffer imaging up to 30 min after

© 2011 Journal of Gastroenterology and Hepatology Foundation and Blackwell Publishing Asia Pty Ltd

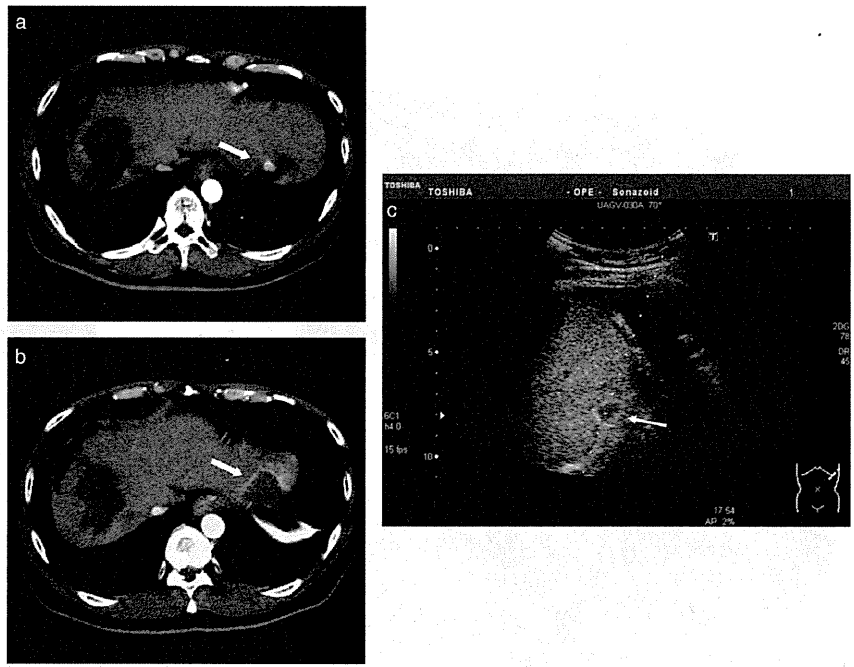

Figure 3 (a) A 52-year-old man with hepatocellular carcinoma. Computed tomography revealed a nodule at the left lateral lobe. (b) This lesion was clearly detected as an enhanced defect in the Kupffer imaging phase. Artificial left pleural effusion was used. (c) The nodule was sufficiently ablated.

Table 2 Comparison of the number of sessions

Variables	Contrast-enhanced ultrasonography group ($n = 291$)	Historical control group ($n = 291$)	*P* value
Maximum diameter (cm)†	1.9 ± 0.8	1.9 ± 0.8	0.94
Number of tumors†	2.1 ± 1.3	2.1 ± 1.3	1.00
Albumin‡	3.5 (3.2–3.9)	3.5 (3.2–3.9)	0.94
Platelet count‡	10.3 (7.8–11.5)	10.5 (7.3–11.3)	0.67
Ablation time per session (min)†	17.2 ± 10.7	15.7 ± 9.6	0.156
Mean number of sessions†	1.33 ± 0.45	1.49 ± 0.76	0.0019

†Mean ± standard deviation.
‡Median (25th–75th percentiles).

Sonazoid injection in cases of insufficient visualization of lesions. Uptake of perfluorobutane in liver parenchyma might have been increased with longer intervals. However, the appropriate interval for observing Kupffer imaging relative to the level of liver function level is not known. Thus, the possibility of detection failure with Sonazoid CEUS should be noted, especially in cases of advanced liver dysfunction.

During the present study, we noticed other limitations of CEUS with Sonazoid. As with conventional US, nodules in certain locations of the liver, such as those immediately below the diaphragm, are difficult to visualize clearly enough for safe and effective RFA even with Sonazoid. For such nodules, the artificial pleural effusion may be useful.[20] Artificial ascites may be useful for the demarcation of nodules near the gastrointestinal tract.[21] Indeed, in the present study, artificial pleural effusion was used in 24.4% of cases and artificial ascites was used in 9.1%, resulting in additional detection of 28 and four nodules, respectively. These techniques are useful in visualizing nodules at certain locations and may enhance the usability of CEUS.

The present study was not a randomized controlled trial directly comparing CEUS with Sonazoid and conventional US, but an analysis of utility of CEUS in RFA, which was analyzed by using historical matched controls. This study design was a compromise with the fact that the final diagnosis was based on dynamic CT, and it was unethical not to use CEUS in case of discrepancy between conventional US and dynamic CT. The historical controls were selected from HCC patients who were treated with RFA after 2004. Since that period, we have performed RFA with the same CT and US apparatuses. Precise comparison of the detection ability and resolution of HCC nodules between conventional US and CEUS will require studies with a design different from the present one.

In conclusion, CEUS with Sonazoid is useful in visualizing HCC nodules that are difficult to detect with conventional US. The number of RFA sessions required for complete ablation of every nodule was decreased in CEUS-assisted RFA, indicating that Sonazoid is a useful supportive agent in RFA. However, the effectiveness of Sonazoid may be compromised in case of severe liver dysfunction.

© 2011 Journal of Gastroenterology and Hepatology Foundation and Blackwell Publishing Asia Pty Ltd